

**EROSION CORROSION AND SYNERGISTIC EFFECTS IN DISTURBED
LIQUID-PARTICLE FLOW**

A thesis presented to
the faculty of the
Fritz J. and Dolores H. Russ
College of Engineering and Technology of
Ohio University

In partial fulfillment
of the requirements for the degree
Master of Science

Ramakrishna Malka

June 2005

This thesis entitled

**EROSION CORROSION AND SYNERGISTIC EFFECTS IN DISTURBED
LIQUID-PARTICLE FLOW**

by
Ramakrishna Malka

has been approved for
the Department of Mechanical Engineering
and the Russ College of Engineering and Technology by

Daniel Gulino
Associate Professor of Chemical Engineering

Dennis Irwin
Dean, Russ College of Engineering and Technology

MALKA, RAMAKRISHNA. M.S. JUNE 2005. Mechanical Engineering

Erosion corrosion and synergistic effects in disturbed liquid-particle flow (72 p.)

Director of Thesis: Daniel Gulino

The present study has been conducted to investigate the interaction between corrosion and erosion processes and quantify synergism in realistic flow environments, across sudden pipe contraction, sudden pipe expansion, and a protrusion. Tests were conducted on a carbon steel, AISI 1018, using 1% sodium chloride (NaCl) solution purged with CO₂ as the corrosive media and silica sand as the erodent. Linear polarization resistance and weight loss are the techniques used for the measurements. The experiments were conducted in a large scale flow loop at a fixed temperature of 34 °C and absolute pressure of 1.2 bar. All experimental conditions were monitored regularly during each experiment. The loop was cleaned before each experiment, and fresh sand was used for each erosion or erosion-corrosion experiment.

The experiments were designed to understand whether erosion enhances corrosion or corrosion enhances erosion and to evaluate the contribution of the individual processes to net synergism. It was observed that erosion enhances corrosion and corrosion enhances erosion, with each contributing to significant synergism. However, the dominant process was the effect of corrosion on erosion.

Approved: Daniel Gulino

Associate Professor of Chemical Engineering

DEDICATION

To

Sujatha Devi Malka and Chokka Rao Malka (my parents)

and

Shilpha Parakala (my wife)

ACNOWLEDGEMENTS

I would like to express my gratitude to my advisor Dr. Daniel Gulino and co-advisor Dr. Srdjan Nestic for their continuous academic and moral support. Their attitude towards everything has inspired me and always encouraged me to perform better in every aspect. This thesis is a tribute to their immense patience, exceptional guidance, and continuous mentorship during my entire stay at the Ohio University.

I would like to acknowledge my indebtedness to Mr. Bruce Brown, Dr. Sandra Hernandez, and Dr. Khairul Alam for their priceless suggestions.

I would also like to thank the technical staff at the Institute for Corrosion and Multiphase Technology, including Mr. Al Schubert and Mr. John Goettge, secretary Debbie Taylor, and co-workers: Shilpha Parakala, Marc Singer, Daniel Mosser, Alvaro Camacho, and Kunal Chokshi for providing a wonderful research environment.

I would also like to acknowledge the contribution of a consortium of companies whose continuous financial support and technical guidance made this research at the Ohio University Institute for Corrosion and Multiphase Technology possible.

TABLE OF CONTENTS

TABLE OF CONTENTS.....	6
CHAPTER 1 INTRODUCTION.....	9
CHAPTER 2 LITERATURE REVIEW.....	11
CHAPTER 3 RESEARCH OBJECTIVES AND TEST MATRIX.....	14
Test Matrix.....	14
Carbon steel material composition.....	15
CHAPTER 4 DETAILS OF THE ERODENT USED.....	18
CHAPTER 5 EXPERIMENTAL SETUP.....	19
Experimental setup.....	19
Test Section Design.....	20
Measurement Techniques.....	24
CHAPTER 6 COMPUTATIONAL FLUID DYNAMIC SIMULATIONS.....	26
CHAPTER 7 EXPERIMENTAL PROCEDURES.....	31
CHAPTER 8 EXPERIMENTAL RESULTS AND DISCUSSION.....	35
Pure corrosion experiments.....	35
Pure erosion experiments.....	38
Erosion-corrosion experiments.....	43
Data analysis.....	47
Discussion.....	53
Future work.....	57
CHAPTER 9 CONCLUSIONS.....	59
REFERENCES.....	60
APPENDIX A CALCULATIONS AND ANALYSIS OF LPR DATA.....	63
Analysis of LPR data.....	63
APPENDIX B WEIGHT LOSS CALCULATIONS.....	65

APPENDIX C	EXPERIMENTAL UNCERTAINTY ANALYSIS	66
APPENDIX D	CFD SETUP	70

LIST OF TABLES

Table I. Pure corrosion test matrix.....	14
Table II. Pure erosion test matrix.....	15
Table III. Erosion-corrosion test matrix.....	15
Table IV. Composition of the specimen material	17

LIST OF FIGURES

Figure 1 Large ring, used in the larger pipe section (I.D = 4 inch, O.D = 4.25 inch, width = 0.75 inch).....	16
Figure 2. Constriction specimen, used at the pipe contraction (I.D = 2.47 inch, O.D = 4.25 inch, width = 1/12 inch).....	16
Figure 3. Small ring, used in the smaller pipe section (I.D = 2.47 inch, O.D = 2.75 inch, width = 0.75 inch).....	16
Figure 4. Size distribution of the sand particles.....	18
Figure 5. Process instrumentation diagram of the experimental flow loop	19
Figure 6. Isometric view of the test section	21
Figure 7. Cut sectional view of the test section showing the pipe contraction.....	22
Figure 8. Cut sectional view of the test section showing a protrusion	22
Figure 9. Cut sectional view of the test section showing the pipe expansion.....	23
Figure 10. Test section in place during the experiment	23
Figure 11. Close-up view showing how electro-chemical measurements are taken	24
Figure 12. Velocity profile of the fluid across the test section	26
Figure 13. Particle flow pattern across the sudden pipe contraction	27
Figure 14. Particle flow pattern across a protrusion	28
Figure 15. Particle flow pattern across sudden pipe expansion	29
Figure 16. Three dimensional simulation of the fluid flow, colored by turbulent kinetic energy.....	30
Figure 17. pH meter with electrode	31
Figure 18. Calibrated pressure gauge attached to the tank	32
Figure 19. Polishing tools that fit onto a drill press to polish ring-like specimens.....	32
Figure 20. Adjustable sampling port to measure sand concentration	32
Figure 21. Heater attached to the tank to maintain temperature	33
Figure 22. Pure corrosion rate across the flow disturbances (pH 4, P _{CO2} 1.2bar, 24 hrs). 35	
Figure 23. Pure corrosion rate across the flow disturbances – second attempt (pH 4, P _{CO2} 1.2bar, 24 hrs)	36

Figure 24. Variation of pure corrosion rate across the flow disturbances with time	37
Figure 25. Pure erosion rate across the flow disturbances (pH 7, P _{N2} 1.2bar, 4 hrs, silica sand 2% by weight).....	38
Figure 26. Sand before erosion (35X).....	40
Figure 27. Sand after erosion, 4 hr run (35X).....	40
Figure 28. Sand before erosion (100X).....	41
Figure 29. Sand after erosion, 4hr run (100X).....	41
Figure 30. Sand before erosion (1000X).....	42
Figure 31. Sand after erosion, 4hr run (1000X).....	42
Figure 32. Metal loss across the flow disturbances in erosion-corrosion environment (pH 4, P _{CO2} 1.2bar, 4 hrs, silica sand 2% by weight).....	43
Figure 33. Sand before erosion-corrosion experiment (35X).....	44
Figure 34. Sand after erosion-corrosion experiment, 4hr run (35X).....	44
Figure 35. Sand before erosion-corrosion experiment (100X).....	45
Figure 36. Sand after erosion-corrosion experiment, 4hr run (100X).....	45
Figure 37. Sand before erosion-corrosion experiment (1000X).....	46
Figure 38. Sand after erosion-corrosion experiment, 4hr run (1000X).....	46
Figure 39. Average pure corrosion rate across the flow disturbances (pH 4, P _{CO2} 1.2bar, 24 hrs).....	47
Figure 40. Average pure erosion rate across the flow disturbances (pH 7, P _{N2} 1.2bar, 4 hrs, silica sand 2% by weight).....	48
Figure 41. Average metal loss across the flow disturbances in erosion-corrosion environment (pH 4, P _{CO2} 1.2bar, 4 hrs, silica sand 2% by weight).....	49
Figure 42. Comparison of pure corrosion (pH 4, P _{CO2} 1.2bar, 24 hrs) and corrosion rate in erosion-corrosion (pH 4, P _{CO2} 1.2bar, 4 hrs, silica sand 2% by weight).....	49
Figure 43. Comparison of pure erosion (pH 7, P _{N2} 1.2bar, 4 hrs, silica sand 2% by weight) and erosion in combined erosion-corrosion (pH 4, P _{CO2} 1.2bar, 4 hrs, silica sand 2% by weight).....	50
Figure 44. Increment in erosion and corrosion due to their interactions.....	52
Figure 45. Net synergism across the flow disturbances.....	52
Figure 46. polished specimen before exposure (3000 X).....	53
Figure 47. Specimen after erosion (1000X).....	54
Figure 48. Specimen after erosion (3000X).....	54
Figure 49. Specimen exposed to erosion-corrosion environment (1000X).....	55
Figure 50. Specimen exposed to erosion-corrosion environment (3000X).....	56
Figure 51. Specimen after pure corrosion ²⁹ (1000 X).....	56

CHAPTER 1 INTRODUCTION

Corrosion is a material degradation process which occurs due to chemical or electro-chemical action, and erosion is a mechanical wear process (e.g. impact of solid particles).¹ When these two processes act together the conjoint action of erosion and corrosion in aqueous environments is known as erosion-corrosion. This phenomenon is known to cause premature failure in the equipment used in engineering applications. In other words, the combined effects of erosion and corrosion can be significantly higher than the sum of the effects of the processes acting separately.^{1,2,3} This net effect is called synergism. As proposed by many researchers, this net effect is due to the enhancement of corrosion by erosion and/or enhancement of erosion by corrosion.⁴

In oil and gas production systems, sand is encountered and produced along with corrosive liquids and gases. Prediction of material loss in these kind of environments is difficult because of the synergistic effects due to the complex interactions of erosion and corrosion. Hence erosion-corrosion due to sand is an increasingly significant problem in petroleum production.

Synergism was not well quantified or clearly understood in the past because of the lack of detailed knowledge of the separate kinetics of pure erosion and pure corrosion.³ There are very few studies in which synergism was quantified,⁴⁻⁸ however, most of the work was carried out using jet impingement apparatus or rotating cylinder electrode systems in which the flow patterns or hydrodynamics are way different from reality.¹⁰ Very little work was done using flow loops.^{11,12} It was not possible to separate the damage due erosion and corrosion in a combined erosion-corrosion process, and hence it

is still unclear whether corrosion enhancement due to erosion or erosion enhancement due to corrosion, if either, is dominant.

Erosion is mostly seen at the flow disturbances such as valves, fittings, bends, etc.¹³ This work has been carried out with the aim of clearly understanding the erosion-corrosion phenomenon in realistic environments. Experiments are conducted in a flow loop simulating flow disturbances, including sudden pipe contraction, protrusion and sudden pipe expansion.

Computational fluid dynamics (CFD) is currently one of the most sophisticated and promising approaches for simulating realistic flow patterns in a wide set of research and industrial applications.¹⁴ Hence in order to better understand the flow patterns, simulations were done using FLUENT 6.0.

CHAPTER 2 LITERATURE REVIEW

The corrosion of steel by carbon dioxide (CO₂) is a significant problem in oil production and natural gas treatment facilities and can occur at all stages of production, from down hole to surface processing equipment. Capital and operational expenditures, as well as health, safety, and the environment of the petroleum industry are enormously affected by corrosion.¹⁵ The presence of CO₂ gas in the aqueous phase (CO₂ saturated aqueous solution) in contact with the surface of the metal leads to corrosion and consequent failures. CO₂ corrosion is an electrochemical process (with the details given elsewhere¹⁵) with the overall reaction mechanism as,



Thus, CO₂ corrosion leads to the formation of a corrosion product, iron carbonate (FeCO₃), which, when precipitated, could form a protective or a non-protective layer, depending on several environmental conditions such as iron concentration, pH of the solution, temperature, and partial pressure of CO₂ in the solution.

The presence of sand in the oil produced provides many challenges for the oil and gas industry, and sand management has become increasingly significant as wells with sand became more prominent.¹⁷ Some of the concerns include sand settling, sand separation, and erosion. Material degradation due to the mechanical action of sand particles is known as erosion and is one of the primary concerns. Even small amounts of entrained sand (as little as a few pounds per day), can cause severe damage to equipment at high production velocities.¹⁸ Erosion consists of two types of wear, deformation and cutting.¹⁹ When a solid particle strikes a surface, the local area will be elastically

deformed and subsequently removed, which is known as deformation wear. Cutting wear follows shearing of the surface as a result of oblique collisions similar to a milling cutter. Until recently, the basic premise of most models in the literature was that erosion is a micro cutting mechanism that can be analytically described by an equation of motion of impacting solid particles. Scanning Electron Microscopy (SEM) results established that the process is a sequential extrusion, forging, and fracture phenomenon, and rarely does micro cutting occur. In other words, plastic deformation will occur followed by repeated impacts which results in deformation hardening of the surface layers until they fracture. This is called the platelet mechanism of erosion and was proposed by Levy.²⁰ There has been extensive work done in understanding the erosion mechanisms resulting in many models as reviewed by Ludema and Meng.²¹ They reviewed 98 mathematical erosion models which used 33 variables. No model used more than seven variables, and the number of constants each model used ranged from one to eight. Though there is no consistent pattern in modeling there exists reasonable understanding of erosion mechanisms. Similarly, the basic CO₂ corrosion reaction mechanisms have been well understood and accepted by many researchers through work done over the past few decades.^{15,22}

Erosion-corrosion is a process of material degradation due to the combined action of erosion and corrosion. The production of both CO₂ and sand is common in petroleum production, and hence erosion corrosion is a significant problem in the oil and gas industry.²² The major challenge is to understand the erosion-corrosion mechanisms resulting from the complex interactions between erosion and corrosion. The joint action

of erosion and corrosion leads to synergistic effects which are due to the effect of erosion on corrosion and vice versa.⁴

There is a significant body of work suggesting that corrosion is enhanced by erosion. It was proposed and accepted by many researchers that the impinging particles remove the deposits or protective layer on the metal surface resulting in continuous exposure of fresh metal surface to the corrosive environment resulting in higher corrosion rates.^{4,11} Stack, et al. proposed that erosion affects corrosion by removal of surface deposits, increase of local turbulence, and surface roughening and that corrosion has little or no effect on erosion.³ However it was observed by some researchers that corrosion increases erosion.^{24,26} Postlethwaite proposed that the effect of corrosion is to roughen the metal surface which in turn increases the erosion rate because the latter is very sensitive to the impact angle of the solid particles.²⁴ This was seen even when the corrosion rate accounted for less than 10% of the total wear. Matsumura, et al. suggested that erosion can be enhanced by corrosion through the elimination of the work-hardened layer.²⁵ Burstein, et al. proposed that the effect of corrosion on slurry erosion is mainly through detachment of the flakes formed by repeated impacts of solid particles.²⁶

Despite the extensive work done in the past there has been no clear understanding of erosion-corrosion interactions. Also, most of the research work was done in unrealistic flow conditions. Hence, the aim of this work is to study erosion-corrosion due to sand and CO₂, in realistic flow conditions.

CHAPTER 3 RESEARCH OBJECTIVES AND TEST MATRIX

The following were the principal objectives of this research:

1. Investigate the erosion and corrosion interactions in realistic disturbed flow conditions.
2. Perform in-situ electro-chemical measurements in erosion-corrosion conditions to be able to separate the material loss due to the individual erosion and corrosion processes and determine the major mechanism influencing synergism.

Test Matrix

With the aim of quantifying the synergism accurately, the test matrices shown in Table I through Table III were followed. This is a fundamental study intended to investigate the basic erosion and corrosion interactions, and the effect of parameters such as temperature, velocity, corrosivity, and erosivity is out of the scope of this study. Hence the parameters are fixed. A liquid velocity of 2 m/s was selected to ensure that all the sand particles were entrained. A pH value of 4.0 was selected to avoid any film formation.

Table I. Pure corrosion test matrix

Flow type	Single phase
Temperature (°C)	34
CO ₂ partial pressure (bar)	1.2
Liquid velocity (m/s)	2
pH	4

Table II. Pure erosion test matrix

Flow type	Single phase
Temperature (°C)	34
N ₂ Partial pressure (bar)	1.2
Liquid velocity (m/s)	2
Ph	7
Average sand size (micron)	275
Sand concentration (by weight)	2 %

Table III. Erosion-corrosion test matrix

Flow type	Single phase
Temperature (°C)	34
CO ₂ Partial pressure (bar)	1.2
Liquid velocity (m/s)	2
pH	4
Average sand size (micron)	275
Sand concentration (by weight)	2 %

Carbon steel material composition

Carbon steel AISI 1018 was tested in this study. Three different kind of specimens were used as shown in Figure 1 through Figure 3. (Details of the design of the test section where these specimens were used is given in Chapter 5.) Though these specimens meet the specifications of AISI 1018, they were made from different tubes.

The composition of the material for the specimens is given in Table IV.



Figure 1 Large ring, used in the larger pipe section (I.D = 4 inch, O.D = 4.25 inch, width = 0.75 inch)

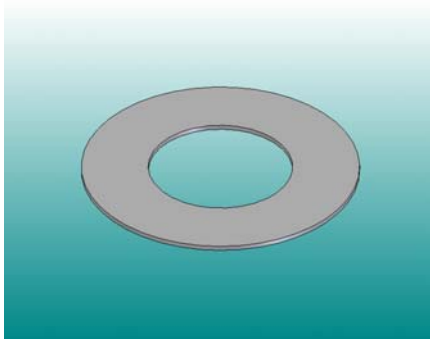


Figure 2. Constriction specimen, used at the pipe contraction (I.D = 2.47 inch, O.D = 4.25 inch, width = 1/12 inch)

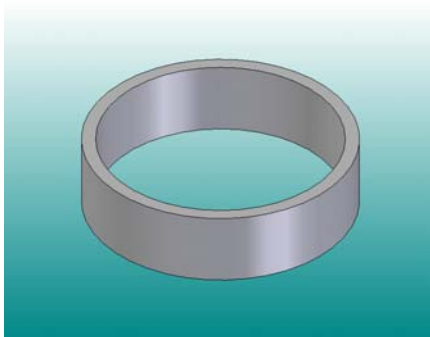


Figure 3. Small ring, used in the smaller pipe section (I.D = 2.47 inch, O.D = 2.75 inch, width = 0.75 inch)

Table IV. Composition of the specimen material

Element	Large ring	Constriction specimen	Small ring
Al	0.039 %	0.031 %	0.027 %
AS	0.007	0.008	0.007
B	0.001	0.001	0.001
C	0.24	0.18	0.24
Ca	0.002	0.000	0.002
Co	0.007	0.005	0.007
Cr	0.026	0.036	0.011
Cu	0.009	0.004	0.024
Mn	0.73	0.72	0.78
Mo	0.012	0.013	0.014
Nb	0.011	0.011	0.011
Ni	0.016	0.017	0.014
P	0.011	0.014	0.011
Pb	0.008	0.008	0.009
S	0.001	0.006	<0.001
Sb	0.023	0.025	0.023
Si	0.022	0.22	0.18
Sn	0.001	0.001	< 0.001
Ta	< 0.001	< 0.001	< 0.001
Ti	< 0.001	< 0.001	< 0.001
V	0.001	< 0.001	< 0.001
Zr	0.003	0.003	0.003

CHAPTER 4 DETAILS OF THE ERODENT USED

The erodent in this study is dry silica sand. The size distribution of the particles is given in Figure 4.

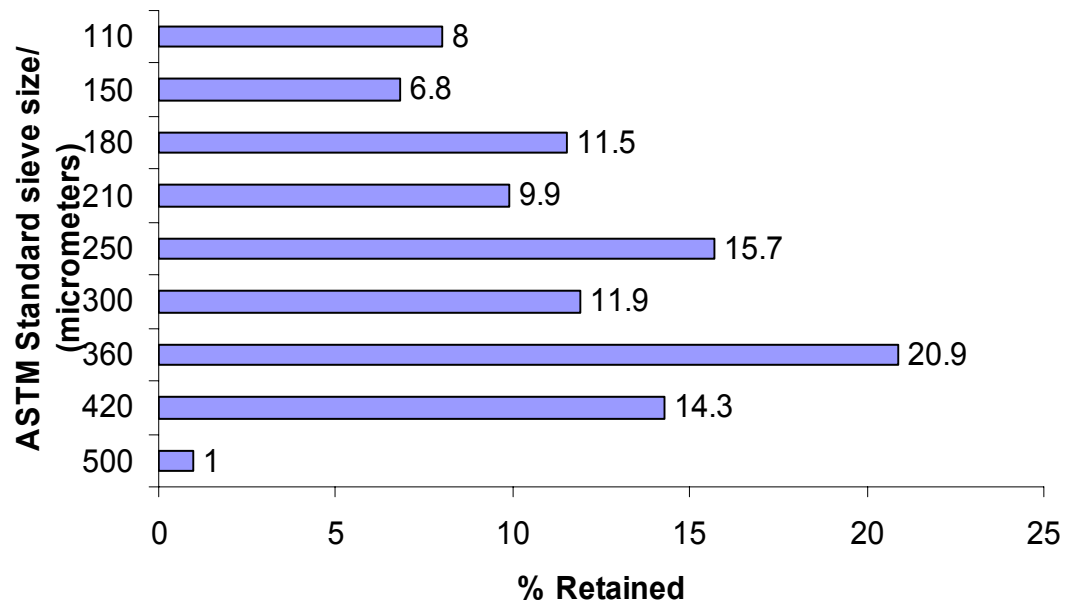


Figure 4. Size distribution of the sand particles

CHAPTER 5 EXPERIMENTAL SETUP

Experimental setup

The experiments were done in a large scale (2000 liter capacity) flow loop to simulate real field conditions. Figure 5 shows the process and instrumentation diagram of the flow loop.

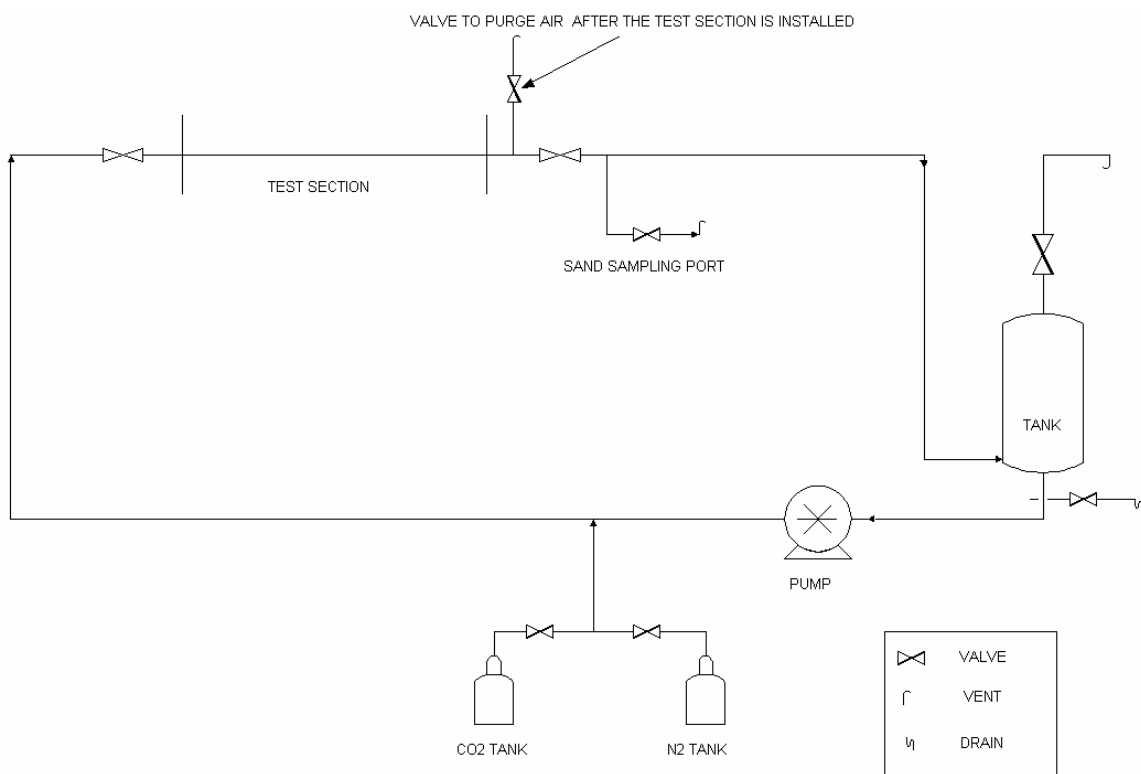


Figure 5. Process instrumentation diagram of the experimental flow loop

The flow loop consisted of a large stainless steel conical bottom tank from which the liquid solution (with or without sand) was drawn using a calibrated positive displacement pump. This pump circulates the liquid or slurry through a 30 foot long, 4

inch diameter PVC pipe that was connected to the tank near the bottom. This creates high turbulence inside the tank sufficient to keep the sand particles moving. There is a provision in the pipe where a newly designed test section can be installed on which it was intended to carry out the erosion-corrosion study. The valves before and after this provision, as can be seen in the Figure 5, help installation and removal of the test section without contaminating the liquid with air. This pipe is also connected to nitrogen and carbon dioxide sources. A thermocouple is installed near the test section for temperature measurement. Sand can be sampled by diverting a portion of the flow using an adjustable sampling port, as shown in Figure 20.

Test Section Design

In order to achieve the above stated research objectives, a unique test section has been designed and developed. The form of the test section enables study across three different geometries that commonly occur in pipeline designs: sudden pipe contraction, sudden pipe expansion, and protrusion. The test section simulates a 4 inch diameter pipe contracting into a 2.47 inch diameter pipe and then expanding into a 4 inch diameter pipe. This gives an area ratio of 2.6 and diameter ratio of 1.61 for larger to smaller pipe sections. The total length of the test section is 54 inches.

The test cell is segmented in order to enable measurements of local weight loss across the flow disturbances. The ring-like specimens, made of the desired material to be tested, slide in to an outer tube made of acrylic, which was chosen because of its transparency and electrical insulation properties.

The specimens are electrically separated using O-rings made of Buna-N, which was selected because it has excellent compression properties, high electrical resistance, and resistance to oxidation, and impact/abrasion. With the help of the outer acrylic tubing and O-rings, it was possible to hold the specimens in compression, and hence good mechanical sealing was achieved. Electrical contact with the individual specimen was made using 10-32 stainless steel screws which go through the outer tube with the help of 10-32 helical inserts embedded in the tubing (Figure 11). With this arrangement, electrochemical measurements can be performed. Figure 6 through Figure 9 are schematic diagrams of the test section, drawn using a software named solid edge. Figure 10 and Figure 11 are the original pictures taken when the test section is put in place.

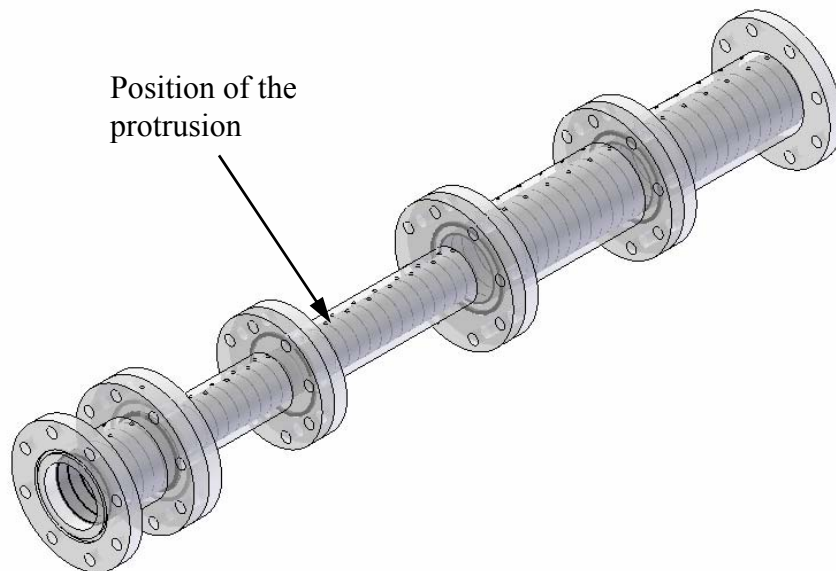


Figure 6. Isometric view of the test section

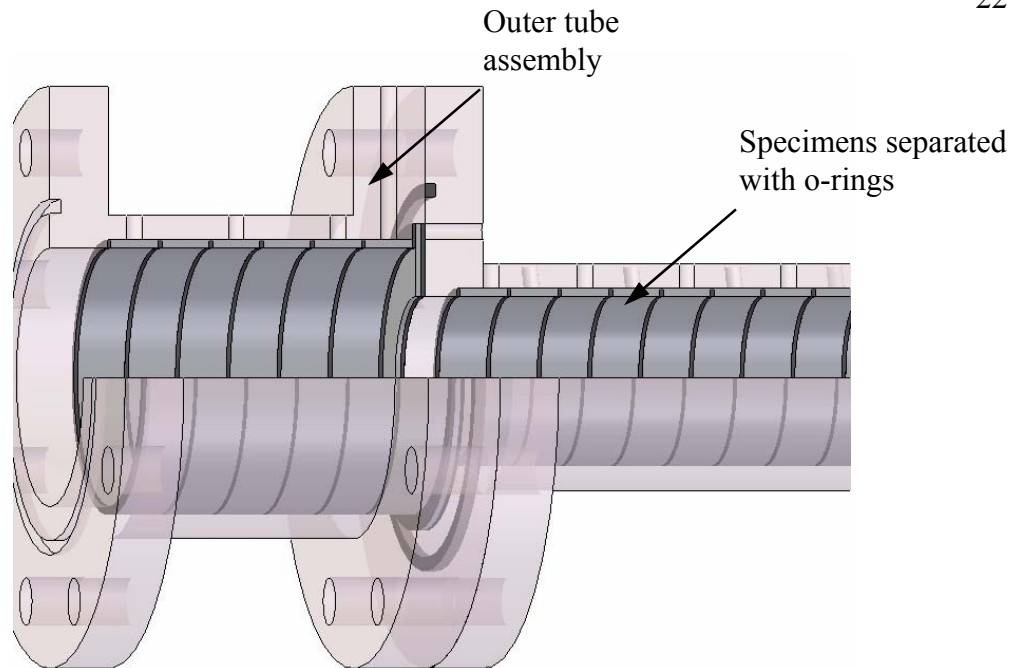


Figure 7. Cut sectional view of the test section showing the pipe contraction

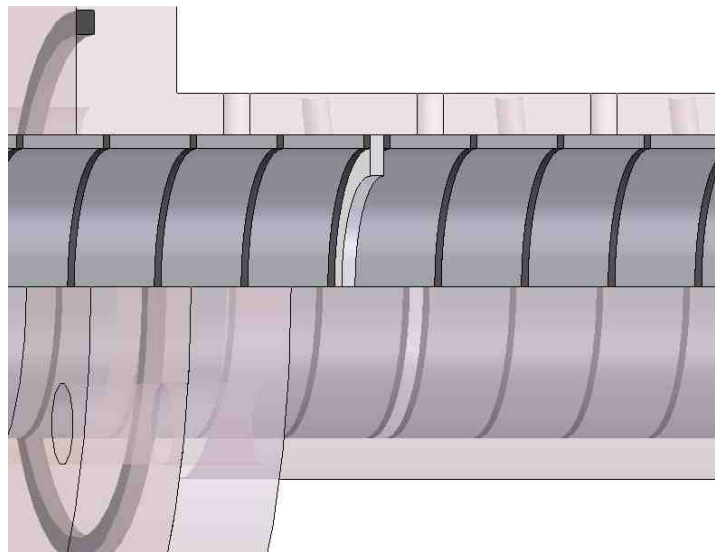


Figure 8. Cut sectional view of the test section showing a protrusion

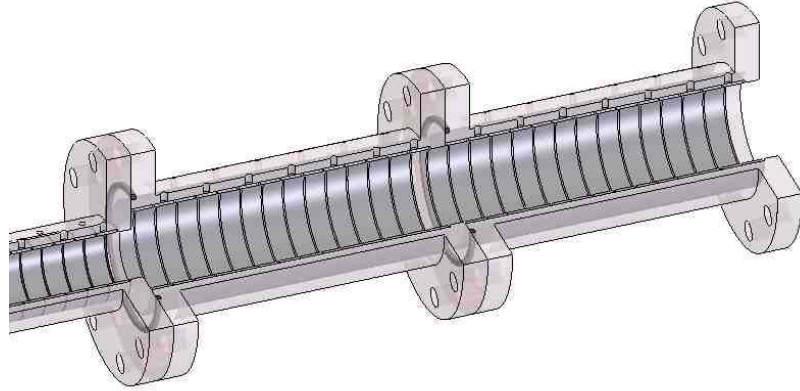


Figure 9. Cut sectional view of the test section showing the pipe expansion

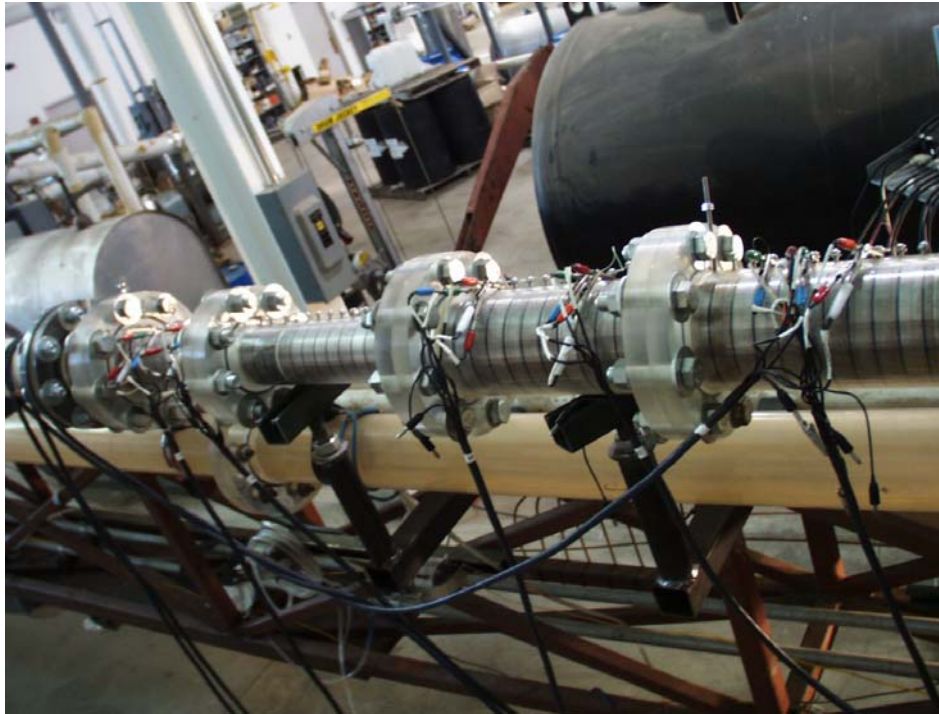


Figure 10. Test section in place during the experiment

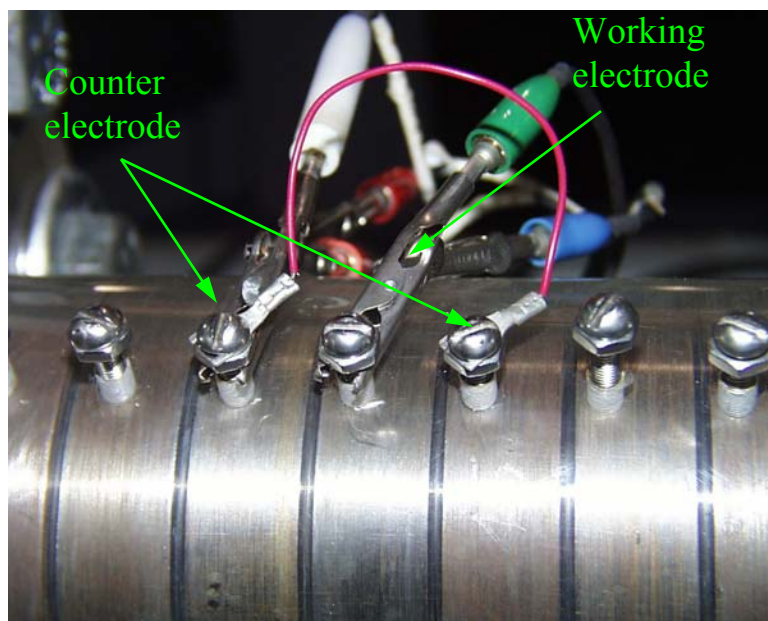


Figure 11. Close-up view showing how electro-chemical measurements are taken

Measurement Techniques

Electrochemical corrosion measurements were performed with a potentiostat connected to a computer. Measurements were taken after the corrosion potential is stabilized (after about 20 minutes). Corrosion rates were measured using the linear polarization resistance (LPR) method following two electrode procedure.²⁸ This technique is used to measure the *in-situ* corrosion rate. The metal sample was polarized ± 5 mV around the corrosion potential during the LPR measurement. The resistance for the current flow measured using the LPR technique was the total resistance, and the solution resistance needed to be compensated for, is measured by the electrochemical impedance spectroscopy (EIS) technique. The equations used to calculate the corrosion rate using LPR are shown in Appendix A. An instrument called a multiplexer was used,

by which it was possible to take LPR measurement for eight specimens at a time. By switching the multiplexer in series, data can be obtained for all the specimens.

The weight loss technique is used to calculate the average material loss. Each polished specimen was weighed using a balance with an accuracy of 1/10th of a milligram before assembling it into the test section. After the experiment, each specimen was cleaned and weighed again. The weight difference gives the average metal loss rate, and the necessary equations are shown in Appendix B.

An experimental uncertainty analysis due to the inherent error in the measurement techniques as well as in the calculations was done, and this is explained in detail in Appendix C.

CHAPTER 6 COMPUTATIONAL FLUID DYNAMIC SIMULATIONS

Computational fluid dynamics simulations of the liquid-particle flow in the test section were done using FLUENT 6.0.20. The liquid phase was water and the solid phase was silica particles. The details of the CFD setup are given in the Appendix D. Pressure and gravitational force values used were 1.2 bar and 9.8 m/s^2 , respectively.

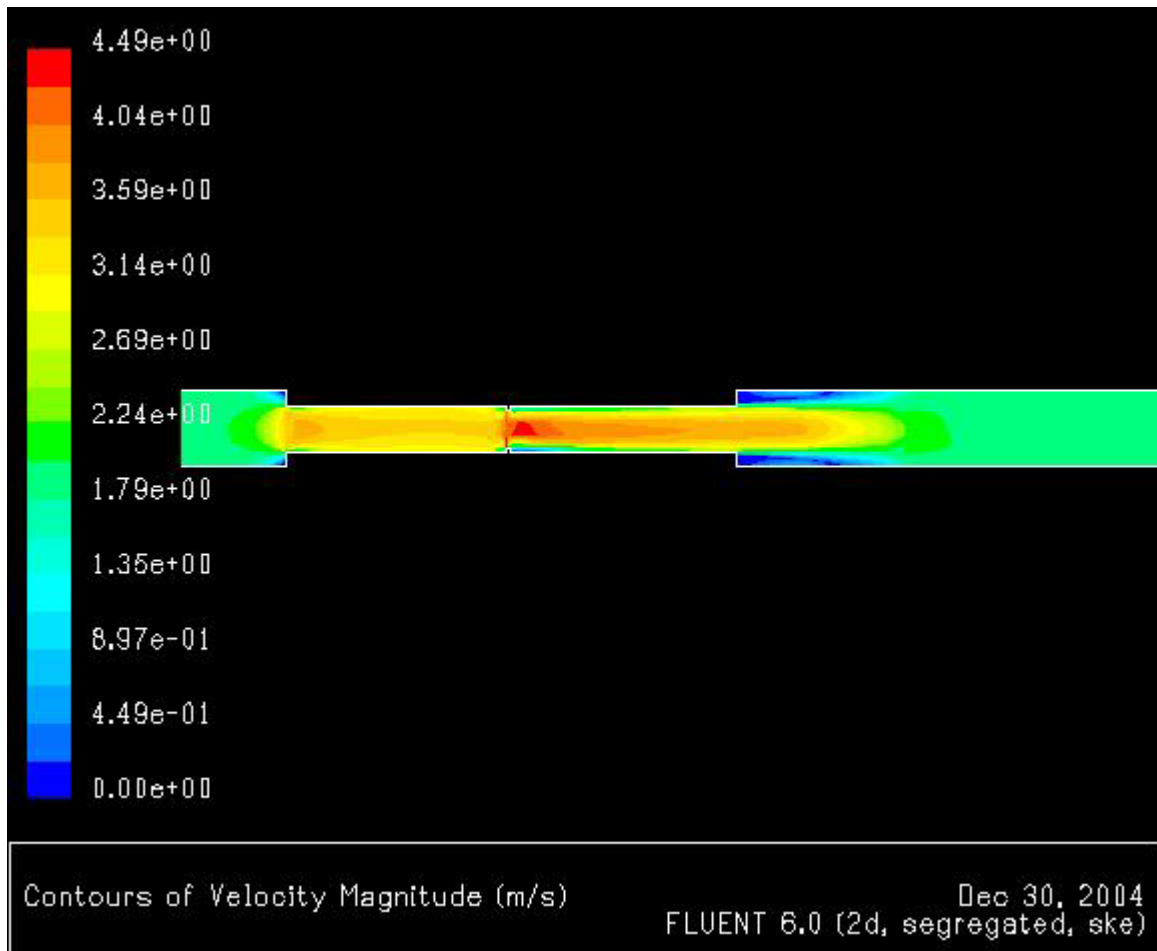


Figure 12. Velocity profile of the fluid across the test section

Figure 12 shows the two dimensional velocity profile of the liquid phase across the flow disturbances in the test section. It is obvious that the velocity and turbulent intensity are greater in the smaller pipe section, and hence high corrosion rates are expected. However, when observed in near wall regions, the velocity is smaller immediately after the flow disturbances. A stagnation zone is seen immediately after the sudden expansion. Since the corrosion is a surface phenomenon, it is expected that the corrosion rate will be low in these regions.

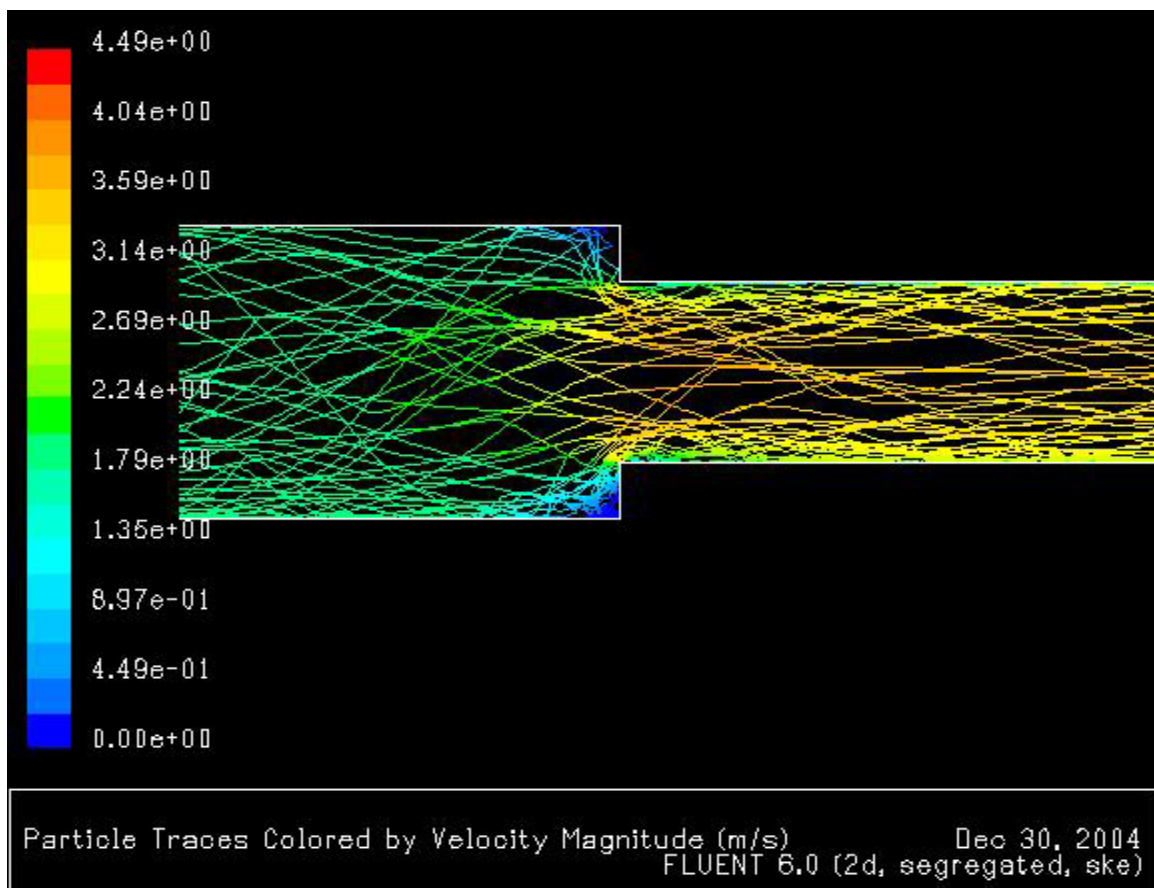


Figure 13. Particle flow pattern across the sudden pipe contraction

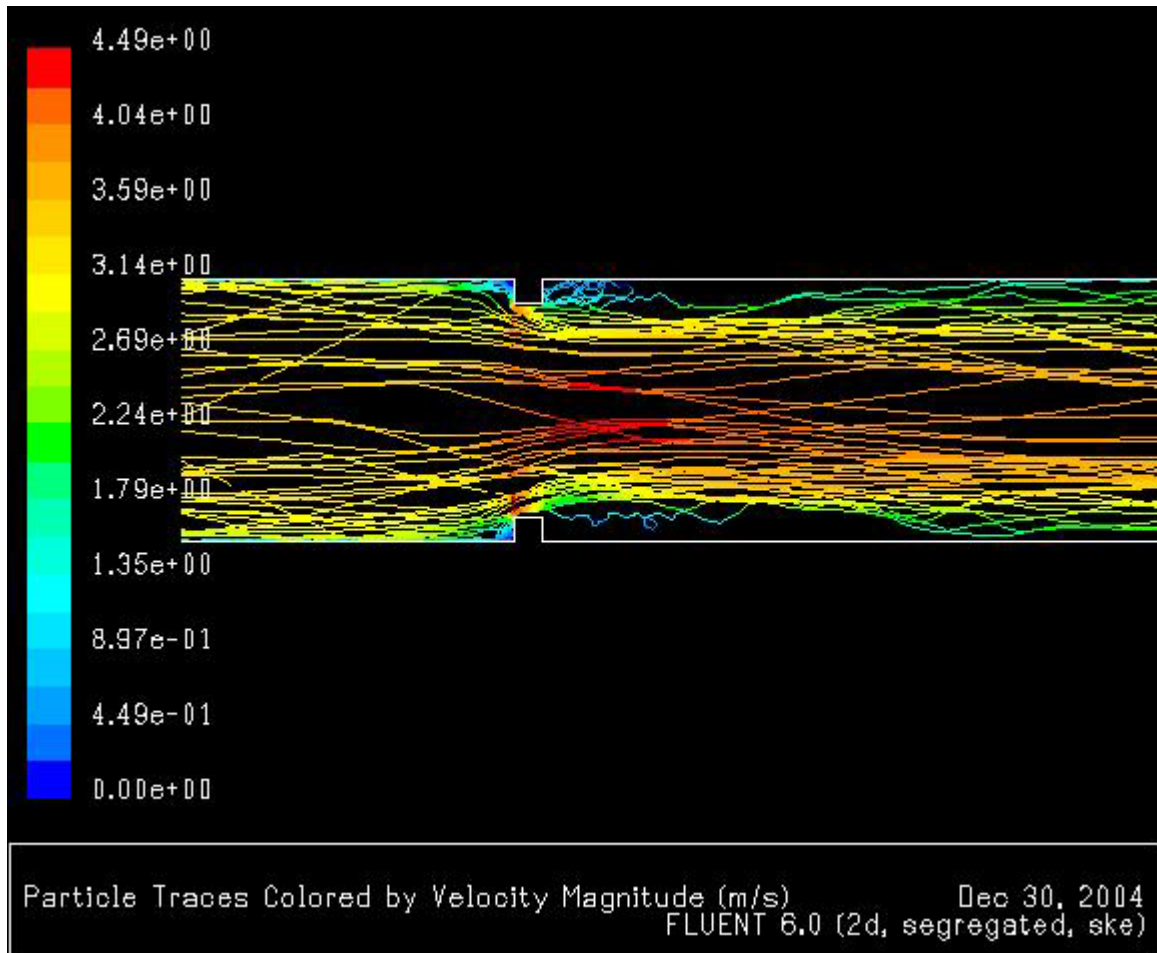


Figure 14. Particle flow pattern across a protrusion

Figure 13 through Figure 15 shows the two dimensional particle flow pattern across the flow disturbances, colored by velocity or kinetic energy. Uniform particle distribution and inlet surface injections have been used. The particles are tracked using a stochastic turbulence model.

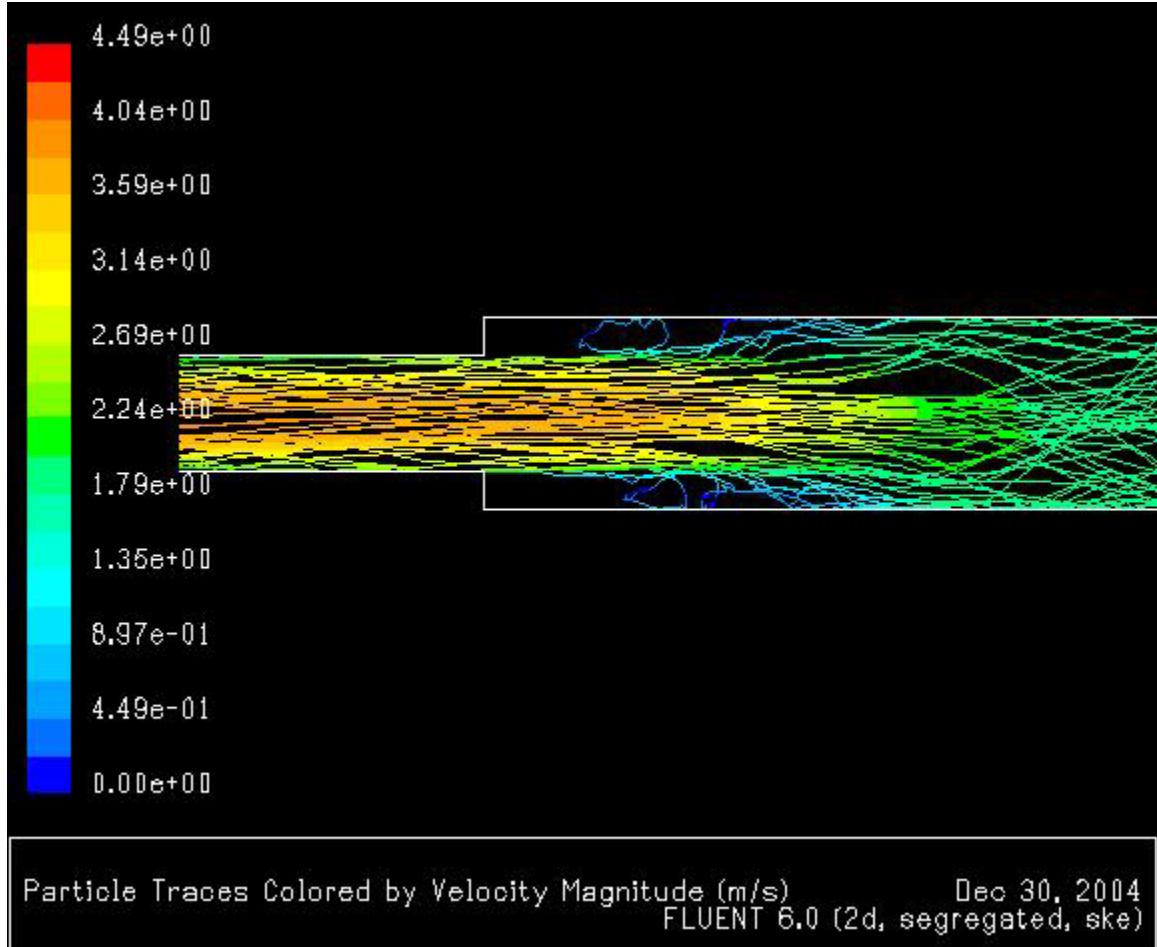


Figure 15. Particle flow pattern across sudden pipe expansion

As seen in these figures, particles have a higher kinetic energy in the smaller pipe section, and hence higher erosion rates were expected. Similarly as explained earlier, this simulation suggests that immediately after the flow disturbances lower erosion rates can be expected.

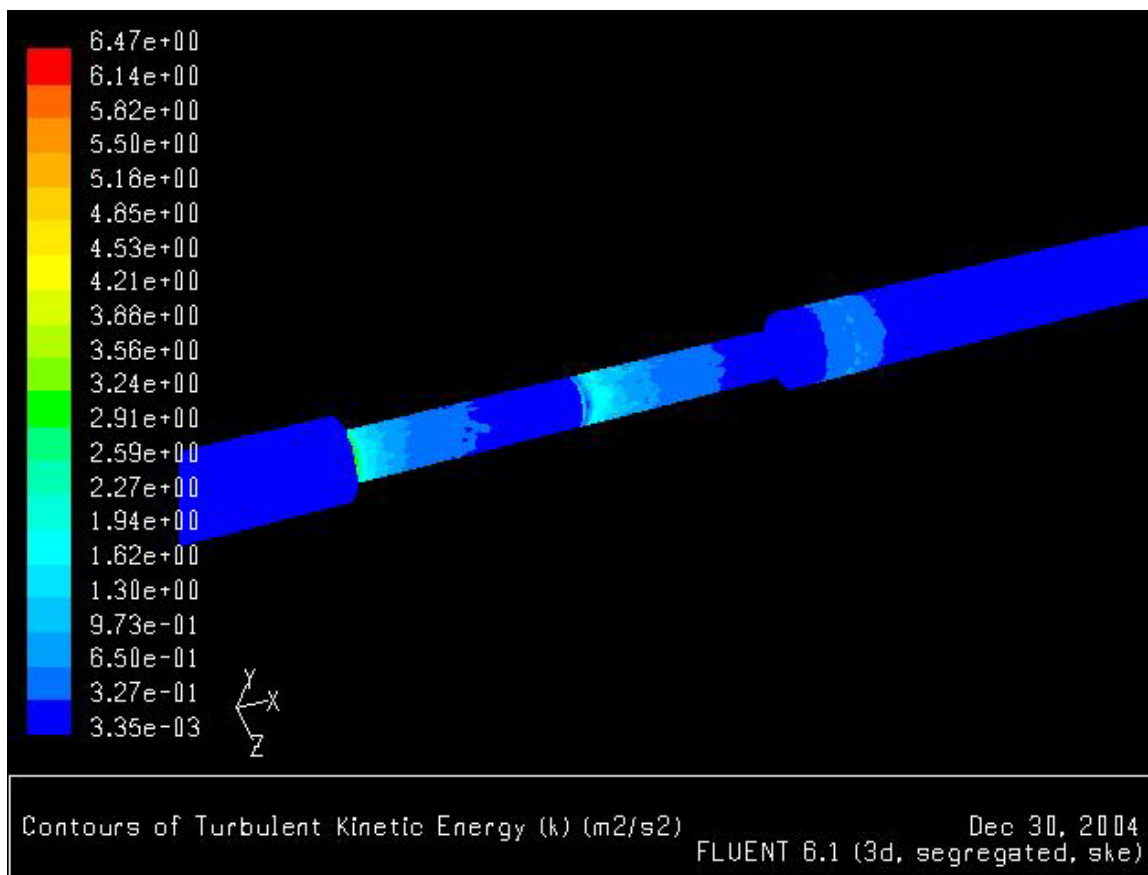


Figure 16. Three dimensional simulation of the fluid flow, colored by turbulent kinetic energy

Figure 16 represents three dimensional simulation of flow colored by turbulent kinetic energy. It can be seen that the flow is more turbulent immediately after the flow disturbance. Hence higher corrosion rates are expected in these regions.

CHAPTER 7 EXPERIMENTAL PROCEDURES

The general procedure for experiments was as follows. The tank/loop with a dummy test section was initially filled with approximately 300 gallons of distilled water with NaCl added to make the solution 1% by weight. The solution was then purged with N_2/CO_2 gas to deoxygenate to < 20 parts per billion (ppb). Heaters were used to maintain the desired temperature. The pH of the solution was adjusted from the equilibrium value to the desired value by adding a calculated amount of deoxygenated sodium bicarbonate solution. The test section was assembled using the specimens polished to 400 grit using the polishing tools as shown in Figure 19. After measuring the concentration of Fe^{2+} the test section was installed and purged with N_2/CO_2 to avoid oxygen contamination. The length of the experimental runs was 4 to 24 hours. During the experiments, parameters such as pH, temperature, and pressure were regularly monitored.

Figure 17 through Figure 21 show the equipment used in the experimentation.



Figure 17. pH meter with electrode



Figure 18. Calibrated pressure gauge attached to the tank

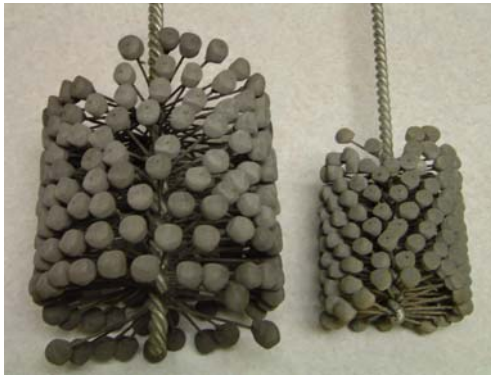


Figure 19. Polishing tools that fit onto a drill press to polish ring-like specimens



Figure 20. Adjustable sampling port to measure sand concentration



Figure 21. Heater attached to the tank to maintain temperature

First, pure corrosion experiments were conducted at pH 4 using 1% NaCl solution pressurized with carbon dioxide (CO_2). Linear Polarization Resistance (LPR) and classical weight loss techniques were used to measure the pure corrosion rate (CR_{PC}) of each specimen across the test section. Second, pure erosion experiments were conducted at pH 7 using silica sand and 1% NaCl solution pressurized with nitrogen. Sand at 2% by weight was added into the loop and was sampled using a sampling port as shown in Figure 20. The weight loss method was used for measuring pure erosion rate (ER_{PE}).

Finally, erosion-corrosion experiments were conducted at pH 4 using sand and 1% NaCl solution pressurized with carbon dioxide (CO_2). For these experiments, the corrosion component (CR_{EC}) was obtained using the LPR technique which measured only the electrochemical metal loss (metal loss due to corrosion only). The erosion component (ER_{EC}) was derived from the difference in total weight loss (WL_{EC}) and the corrosion component. Hence the increment in corrosion due to erosion, increment in erosion due to corrosion, and synergism was obtained by comparing these erosion and corrosion components with the data obtained from pure erosion and corrosion measurements.

Mathematically,

$$\text{Erosion rate component, } ER_{EC} = WL_{EC} - CR_{EC}$$

$$\text{Increment in erosion due to corrosion, } \Delta ER = ER_{EC} - ER_{PE}$$

$$\text{Increment in corrosion due to erosion, } \Delta CR = CR_{EC} - CR_{PC}$$

$$\text{Net synergism, } \Delta Syn = WL_{EC} - (ER_{PE} + CR_{PC}) = \Delta CR + \Delta ER$$

Where,

CR_{PC} = pure corrosion rate

ER_{PE} = pure erosion rate

CR_{EC} = corrosion rate component in combined erosion-corrosion

WL_{EC} = total weight loss in combined erosion-corrosion

CHAPTER 8 EXPERIMENTAL RESULTS AND DISCUSSION

Pure corrosion experiments

Pure corrosion experiment with a repetition was conducted as explained in Chapter 7. The duration of the test was for 24 hours, and the results are shown in Figure 22. The corrosion rate obtained from LPR (Linear polarization resistance) method is the average of five data points taken within the span of the experiment. The deviation bars are the maximum and minimum values obtained.

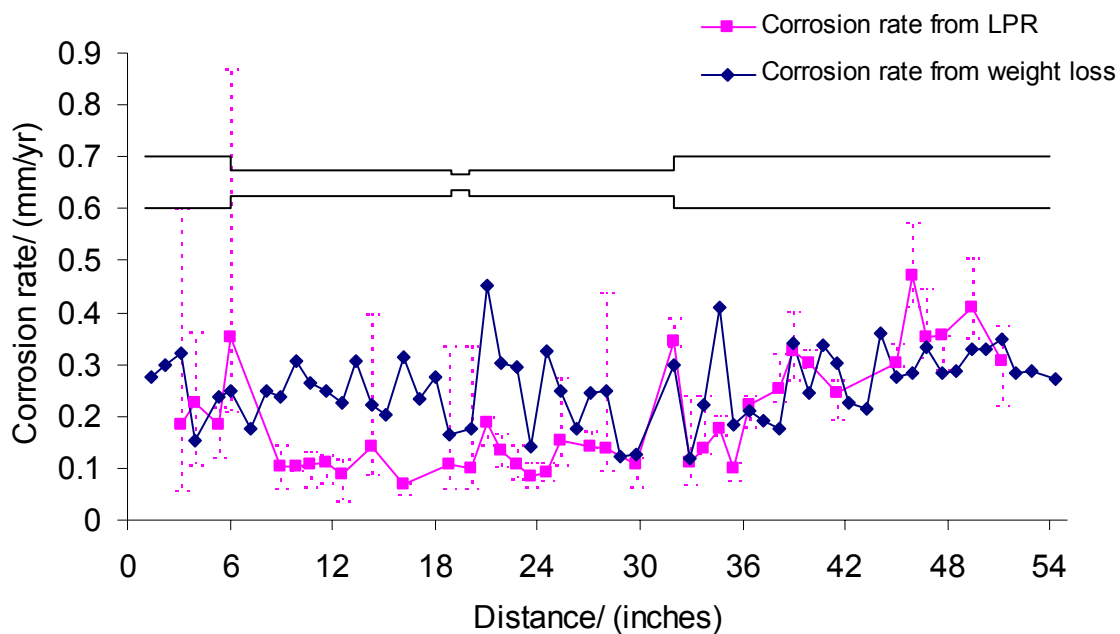


Figure 22. Pure corrosion rate across the flow disturbances (pH 4, P_{CO_2} 1.2bar, 24 hrs)

The corrosion rate varies across the flow disturbances; however, this trend was not as expected because the corrosion rate in the smaller diameter (2.47 inch) section,

with a Reynolds's number of 285,000, is observed to be lower than in the larger diameter (4 inch) section with a Reynolds's number of 181,500. Also, there was considerable variation across the test section; hence, this experiment was repeated and the results are shown in Figure 23.

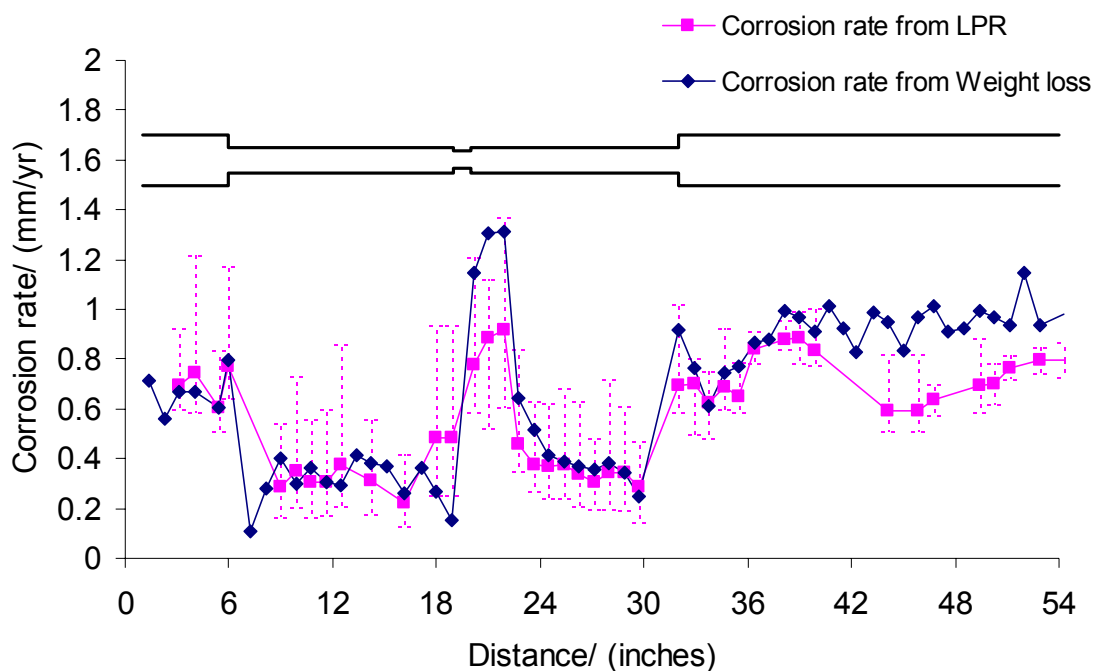


Figure 23. Pure corrosion rate across the flow disturbances – second attempt (pH 4, P_{CO_2} 1.2bar, 24 hrs)

Confidence in the data from this experiment was higher because there was less variation, and it can be clearly seen that the corrosion rates vary depending upon the position along the flow disturbances with the maximum corrosion rate seen next to the protrusion. Though the average corrosion rate in the two experiments differs, the same trend was seen for the smaller and larger diameter sections in both the experiments. This

unexpected trend could be attributed to the fact that the specimens used for the two sections were made from two completely different tubes, each meeting the specifications of AISI 1018. The composition of the materials of the specimens used for smaller and larger pipe sections is given in Table IV. Since the difference is not considerable, it is expected that this trend is due to metallurgical differences in the materials. From the data obtained, it was also observed that the trend of the corrosion rate across the flow disturbances was similar with time. This can be concluded from Figure 24, which shows the LPR data taken for the second experiment approximately every 5 hours. The results from LPR and weight loss agree in both the pure corrosion experiments, suggesting that the design of the test section is successful.

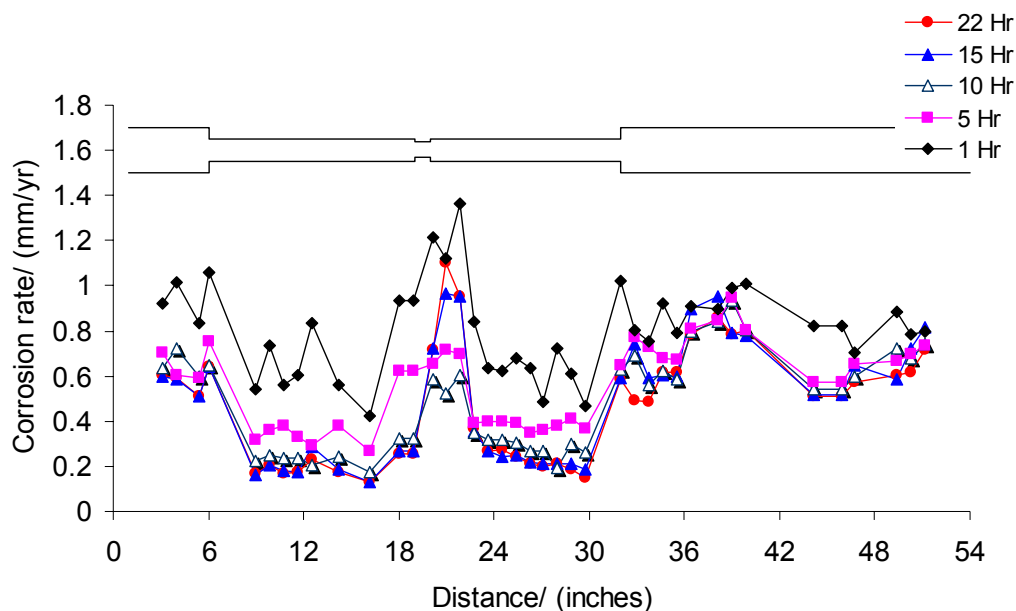


Figure 24. Variation of pure corrosion rate across the flow disturbances with time

Pure erosion experiments

Pure erosion experiment with a repetition was conducted as explained in Chapter 7 so as to minimize the occurrence of any corrosion. The duration of these tests was limited to 4 hrs to minimize the effect of sand degradation with time. Figure 25 shows the results of these experiments and it can be seen they were repeatable.

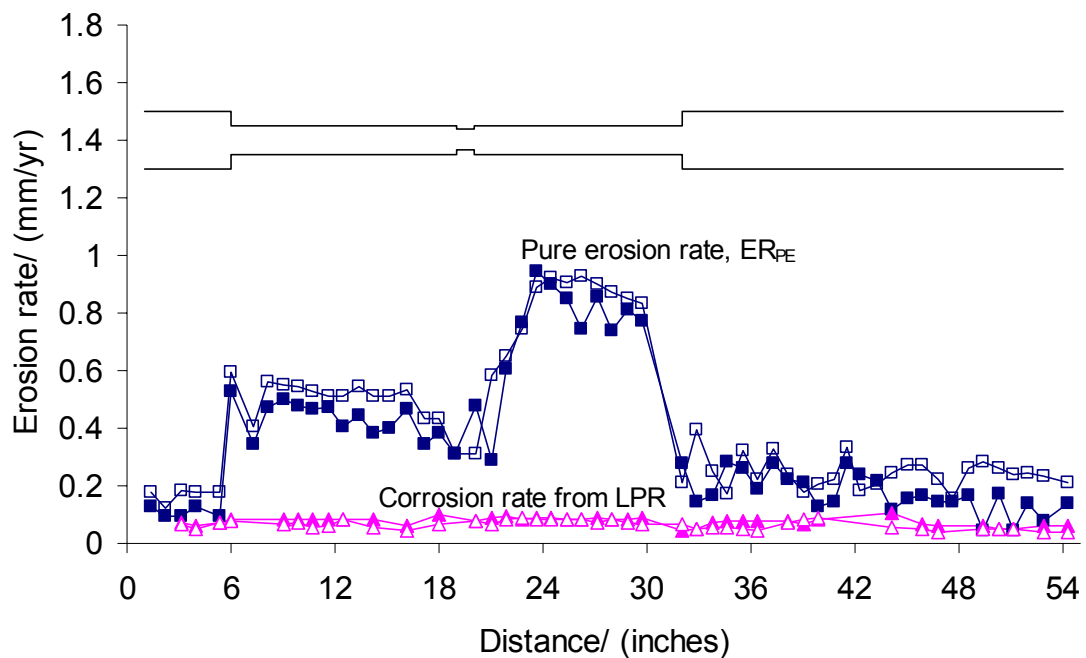


Figure 25. Pure erosion rate across the flow disturbances (pH 7, P_{N_2} 1.2bar, 4 hrs, silica sand 2% by weight)

The erosion rate (ER_{PE}) varied significantly across the flow disturbances, and the higher rates were seen across the protrusion. The low corrosion rate as can be seen from LPR data is constant along the test section in the order of 0.05 to 0.08 mm/yr and can be

ignored for all practical purposes when compared to the erosion rate obtained. The effect of turbulence on erosion rate, as observed in smaller and larger pipe sections, is consistent with the CFD simulation results shown in Chapter 6. This is not true immediately after the flow disturbances, but it is worth noting that erosion is not only dependent on turbulence but also on the angle of impact. Sand was sampled before and after for each experiment, and SEM (Scanning Electron Microscope) pictures of the samples are shown in Figure 26 through Figure 31. The pictures with different magnifications show the sharpness of the particles as well as the surface roughness and confirm that the sand was not degraded within the duration of the experiment.

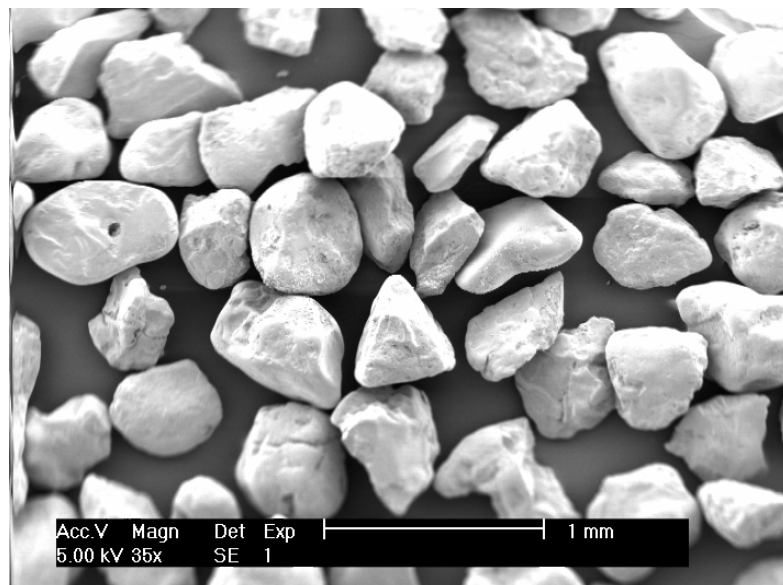


Figure 26. Sand before erosion (35X)

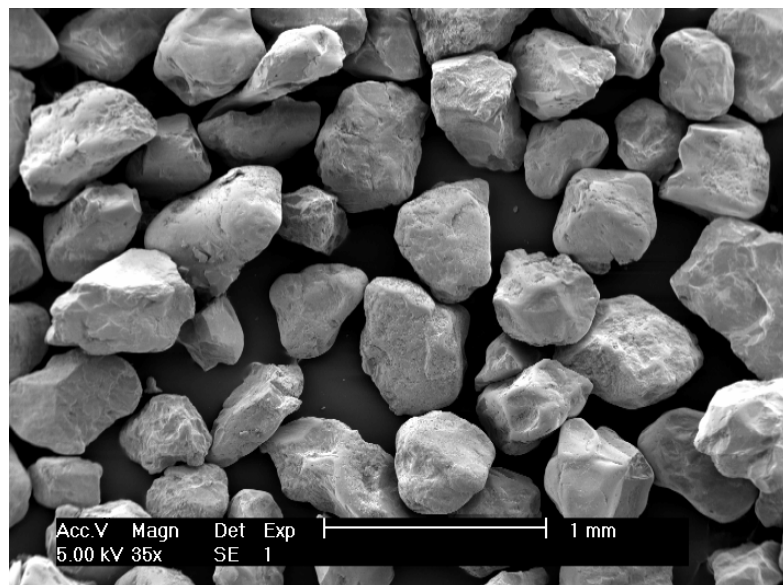


Figure 27. Sand after erosion, 4 hr run (35X)

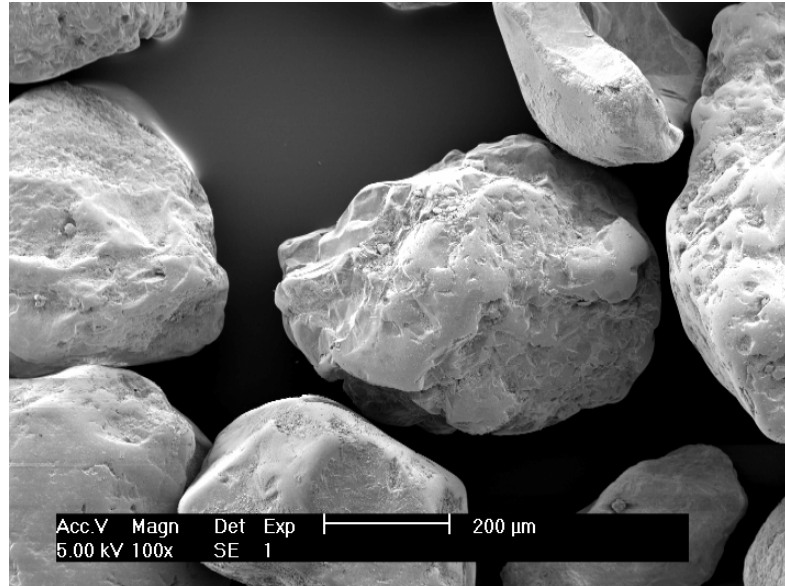


Figure 28. Sand before erosion (100X)

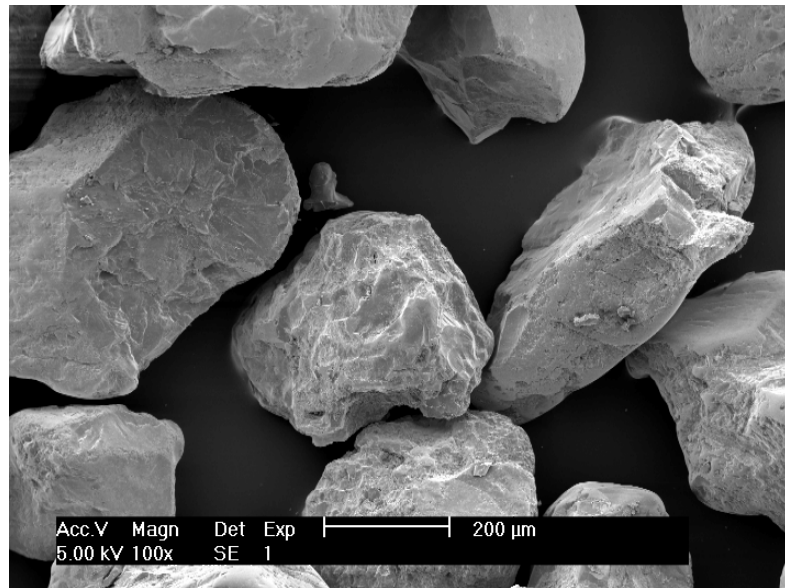


Figure 29. Sand after erosion, 4hr run (100X)

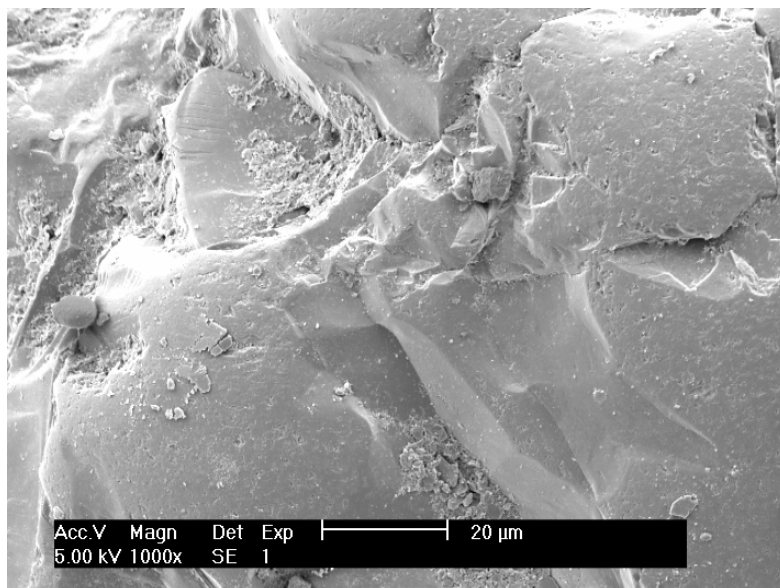


Figure 30. Sand before erosion (1000X)

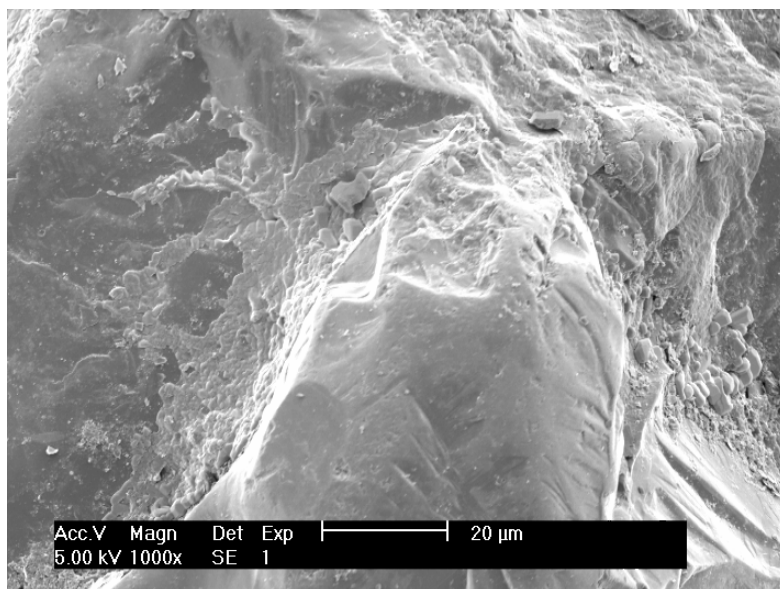


Figure 31. Sand after erosion, 4hr run (1000X)

Erosion-corrosion experiments

Finally, erosion-corrosion experiment, with one repetition, was conducted using silica sand and CO₂ saturated water, at the conditions explained in chapter 7. To minimize the effect of sand degradation the duration of these experiments was also limited to 4 hr. The tests were repeatable as shown in the Figure 32.

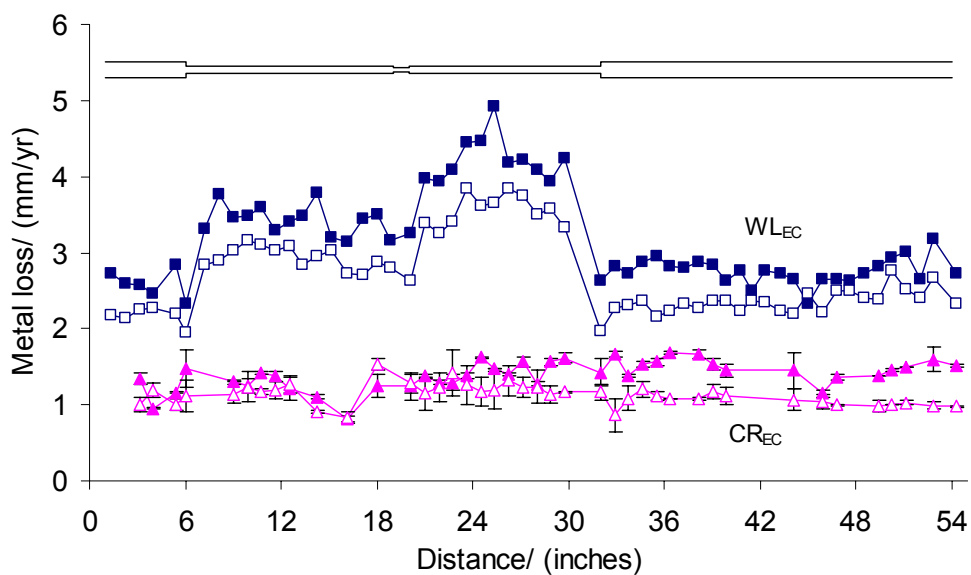


Figure 32. Metal loss across the flow disturbances in erosion-corrosion environment (pH 4, P_{CO₂} 1.2bar, 4 hrs, silica sand 2% by weight)

LPR is an electro-chemical measurement technique and hence detects the material loss only due to corrosion (CR_{EC}), and the weight loss detects the total material loss due to combined erosion-corrosion (WL_{EC}). Sand was sampled before and after for each experiment. SEM pictures of the samples shown in Figure 33 through Figure 38, indicate that sand did not degrade within the experimental duration.

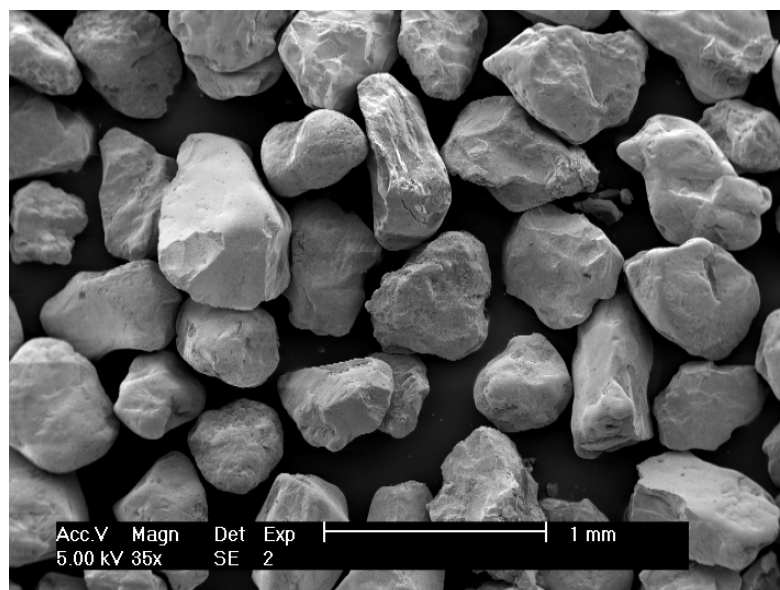


Figure 33. Sand before erosion-corrosion experiment (35X)

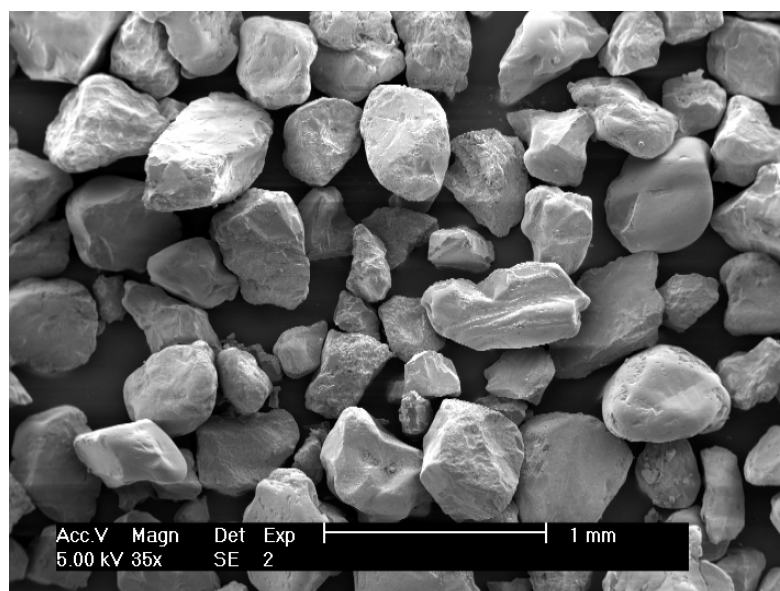


Figure 34. Sand after erosion-corrosion experiment, 4hr run (35X)

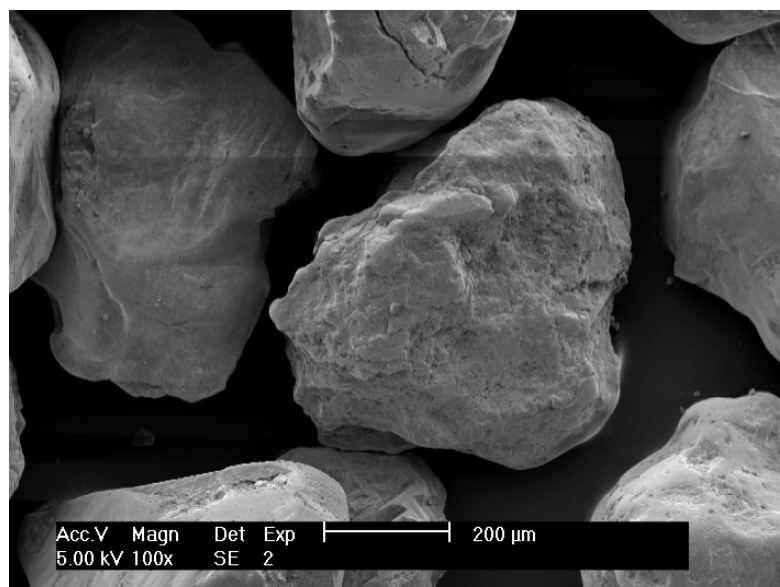


Figure 35. Sand before erosion-corrosion experiment (100X)

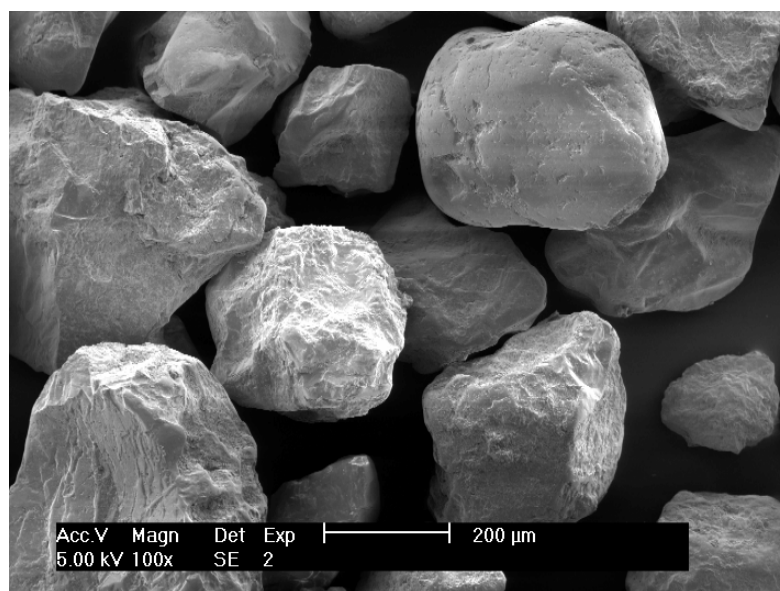


Figure 36. Sand after erosion-corrosion experiment, 4hr run (100X)

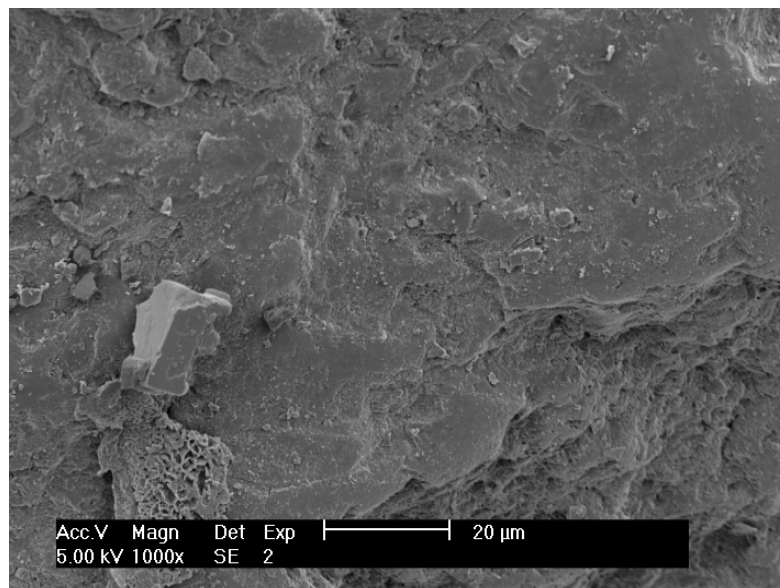


Figure 37. Sand before erosion-corrosion experiment (1000X)

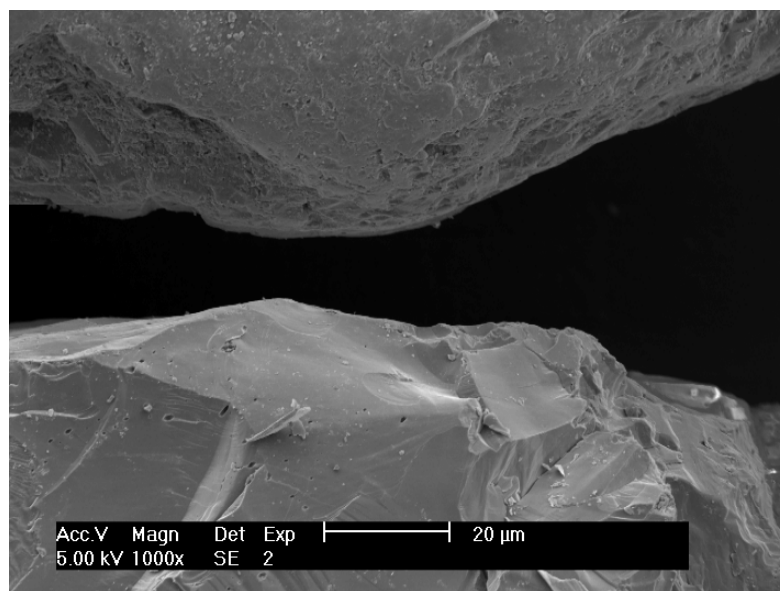


Figure 38. Sand after erosion-corrosion experiment, 4hr run (1000X)

Data analysis

Now that we know the kinetics of pure corrosion, pure erosion, total erosion-corrosion and corrosion component in combined erosion-corrosion, it is possible to calculate the increment in corrosion, increment in erosion and thus total synergism across the flow disturbances as explained at the end of chapter 7.

Pure corrosion rate, CR_{PC} , was considered to be the average of the LPR and weight loss data obtained in the second pure corrosion experiment, considering the second experiment results were more reliable. Figure 39, shows the average pure corrosion rate along the test section.

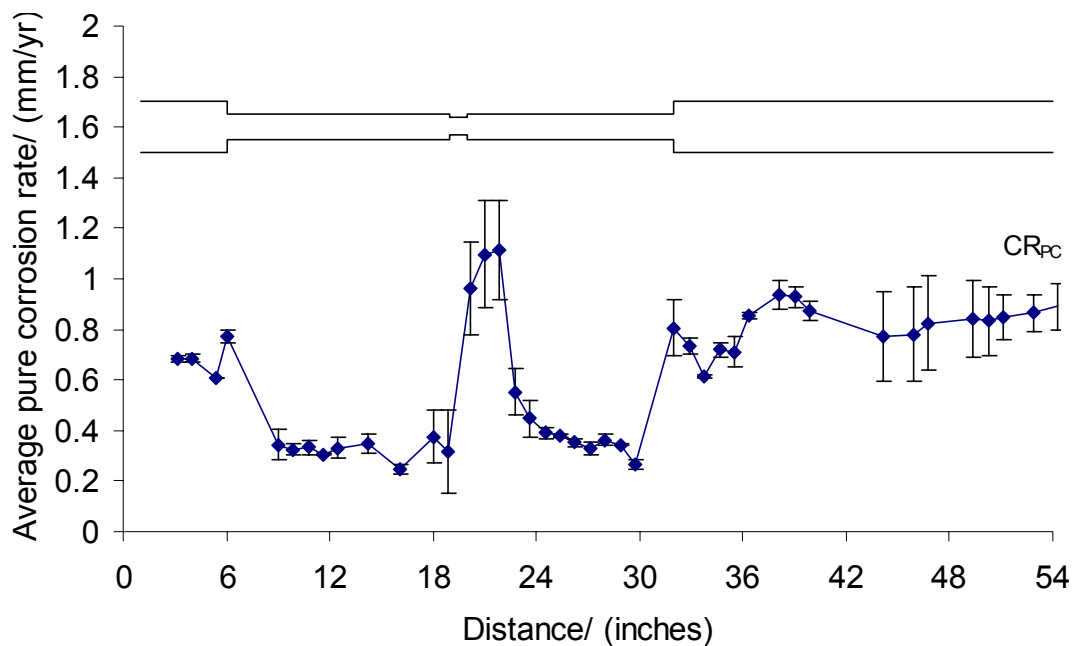


Figure 39. Average pure corrosion rate across the flow disturbances (pH 4, P_{CO_2} 1.2bar, 24 hrs)

Similarly the average pure erosion rate, ER_{PE} , along the test section is shown in Figure 40. This data was obtained from the average weight loss data from the two experiments.

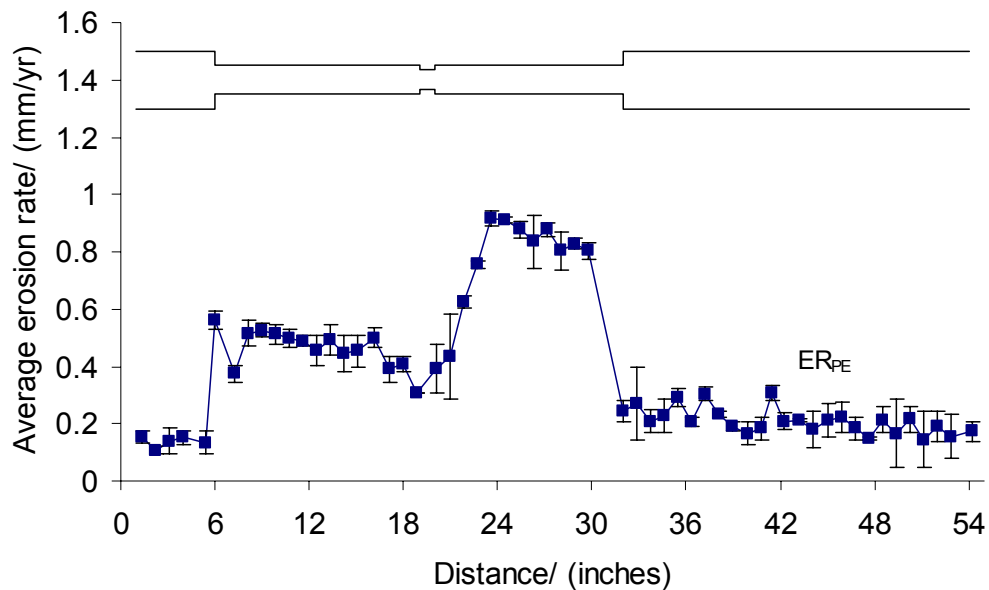


Figure 40. Average pure erosion rate across the flow disturbances (pH 7, P_{N_2} 1.2bar, 4 hrs, silica sand 2% by weight)

The total weight loss, WL_{EC} , is the average of weight loss values taken from the two erosion-corrosion experiments. The corrosion rate in combined erosion-corrosion environment, CR_{EC} , was obtained from the average values of the LPR data taken from the two erosion-corrosion experiments. Figure 41 shows the variation of WL_{EC} and CR_{EC} along the flow disturbances. Figure 42 shows the comparison between the material loss

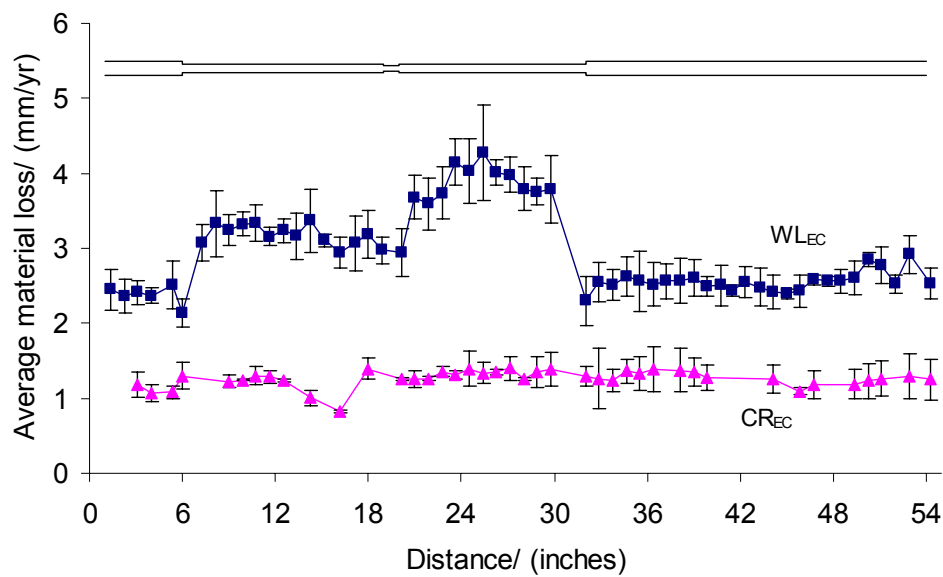


Figure 41. Average metal loss across the flow disturbances in erosion-corrosion environment (pH 4, P_{CO_2} 1.2bar, 4 hrs, silica sand 2% by weight)

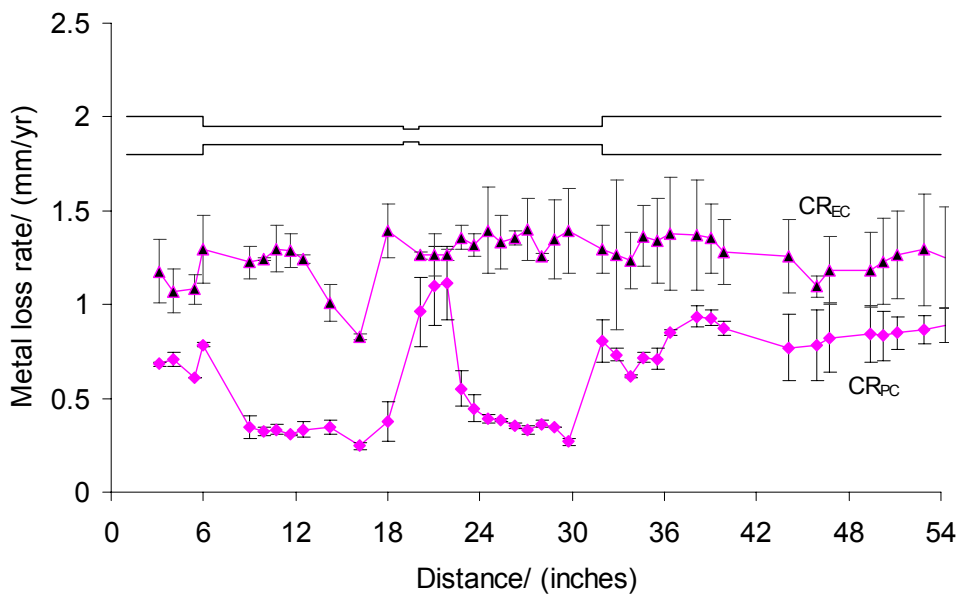


Figure 42. Comparison of pure corrosion (pH 4, P_{CO_2} 1.2bar, 24 hrs) and corrosion rate in erosion-corrosion (pH 4, P_{CO_2} 1.2bar, 4 hrs, silica sand 2% by weight)

due to pure corrosion, CR_{PC} , and the corrosion rate due to erosion-corrosion, CR_{EC} . It can be seen that there is a general increment in corrosion along the test section, however greater increment is seen in the smaller pipe section.

As explained earlier in section, the material loss due to erosion in a combined erosion-corrosion attack can be obtained by using the expression,

$$ER_{EC} = WL_{EC} - CR_{EC}$$

Figure 43 shows the comparison of the pure erosion rate, ER_{PE} and erosion rate in the presence of corrosive environment, ER_{EC} .

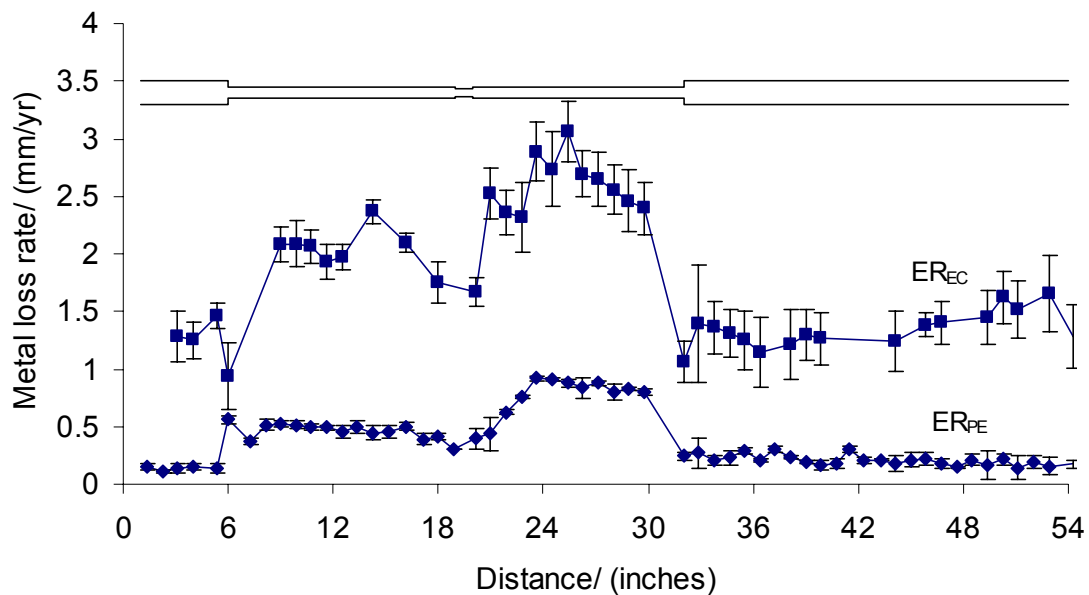


Figure 43. Comparison of pure erosion (pH 7, P_{N_2} 1.2bar, 4 hrs, silica sand 2% by weight) and erosion in combined erosion-corrosion (pH 4, P_{CO_2} 1.2bar, 4 hrs, silica sand 2% by weight)

Hence the increment in erosion due to corrosion, ΔER , and increment in corrosion due to erosion, ΔCR , are calculated as explained in chapter 7, and shown in Figure 44. The average increment in erosion due to corrosion (ΔER) is found to be 3 to 4 times the pure erosion (ER_{PE}). Similarly, the average increment in corrosion due to erosion (ΔCR) is found to be 1 to 2 times the pure corrosion (CR_{PC}). Finally the total synergism is quantified and shown in Figure 45. This synergism (ΔSyn) is found to be 1.5 to 2.5 times the sum of the material loss due to pure erosion and pure corrosion of which the contribution of ΔCR was 30% and of ΔER was 70%, respectively.

Note: The deviation bars shown on all these plots are the maximum and minimum values obtained.

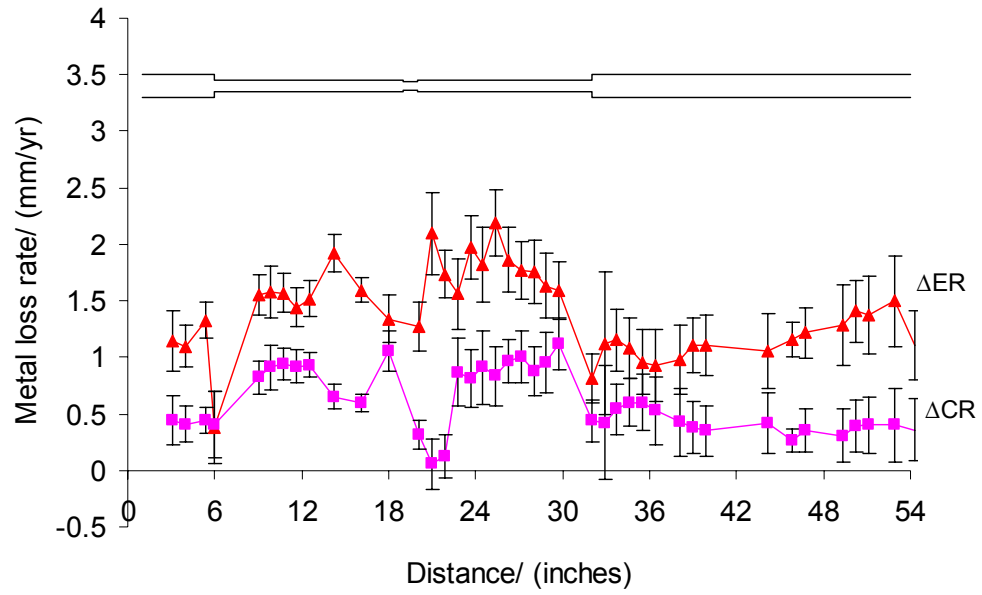


Figure 44. Increment in erosion and corrosion due to their interactions

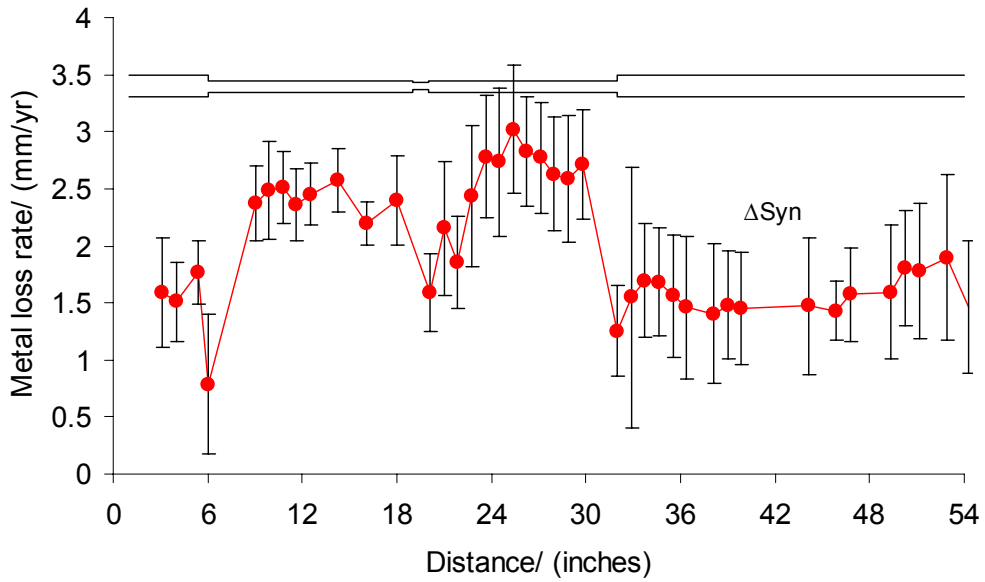


Figure 45. Net synergism across the flow disturbances

Discussion

From the results obtained, it can be concluded that due to the interactions of erosion and corrosion both the mechanisms are enhanced, however the erosion enhancement due to corrosion is larger.

From Figure 42, it can be observed that corrosion is enhanced due to erosion. This effect is observed to be significant in the smaller diameter pipe section, where erosion is relatively higher. This observation supports the speculation made in the past^{3,4,11} that erosion affects corrosion by increase of local turbulence and surface roughening.

From Figure 46 through Figure 48, it can be observed that in pure erosion metal flakes/layers are formed. This supports the platelet mechanism proposed by Levy²⁰ which states that, in erosion, plastic deformation occurs by repeated impacts resulting in deformation hardening of the surface layers until they fracture.

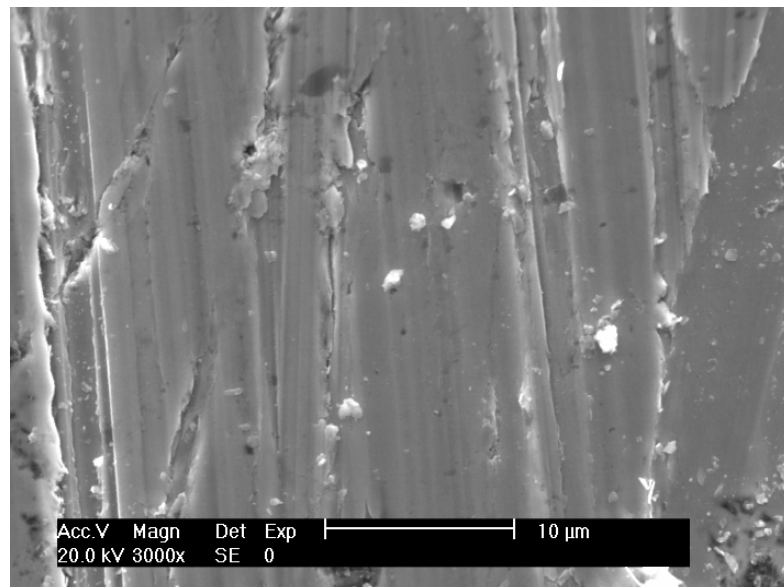


Figure 46. polished specimen before exposure (3000 X)

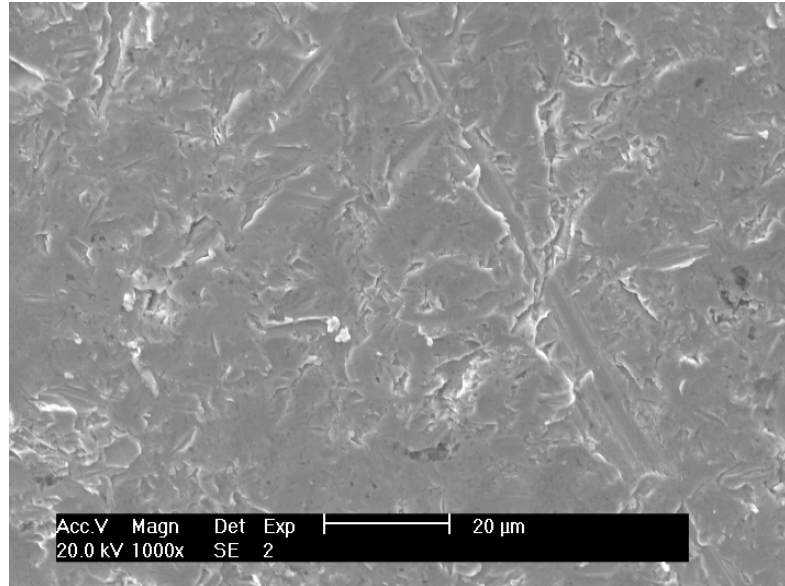


Figure 47. Specimen after erosion (1000X)

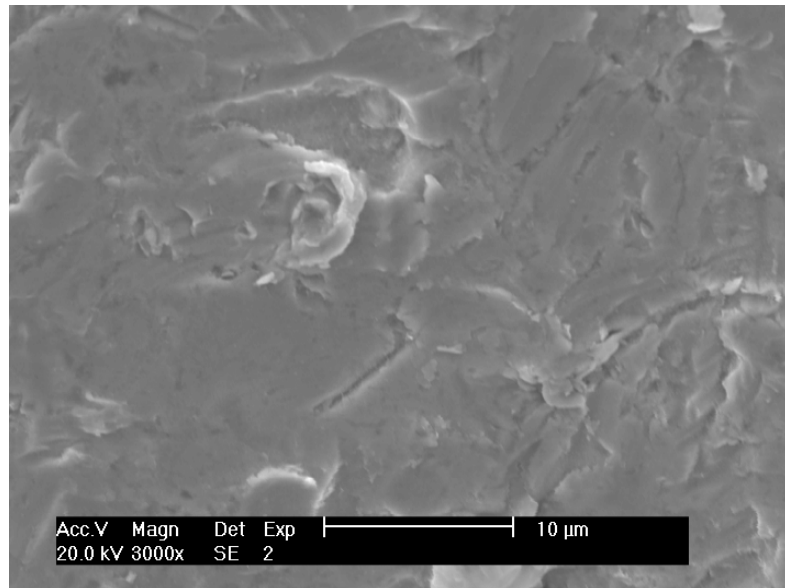


Figure 48. Specimen after erosion (3000X)

From the observations in Figure 49 and Figure 51 it can be concluded that corrosion enhances erosion by the following proposed mechanisms.

1. Corrosion roughens the surface and causes imperfections in the surface which cause the material to be easily removed by subsequent particle impacts.
2. Corrosion enhances pre-detachment of the flakes created due to the repeated particle impacts. It is expected that fewer particle impacts are needed to detach the flakes in the presence of corrosion.

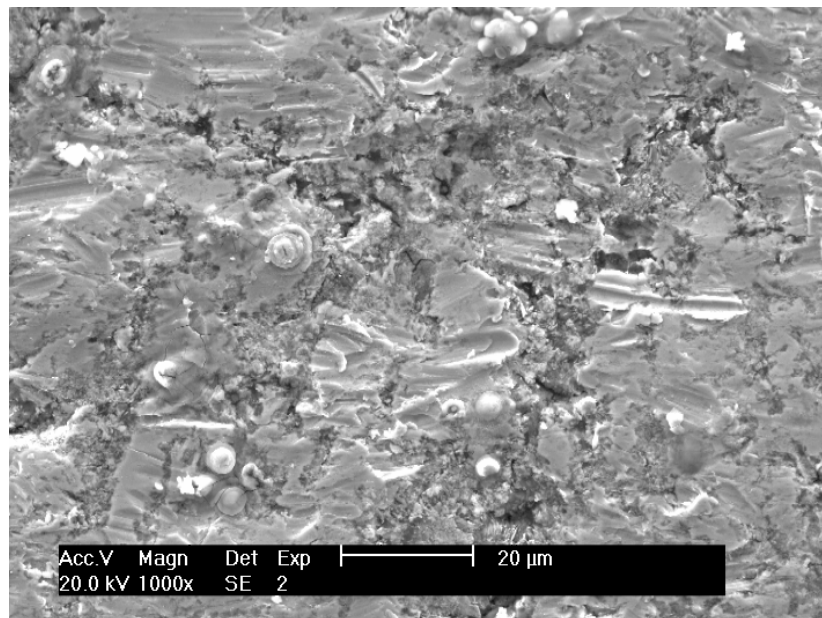


Figure 49. Specimen exposed to erosion-corrosion environment (1000X)

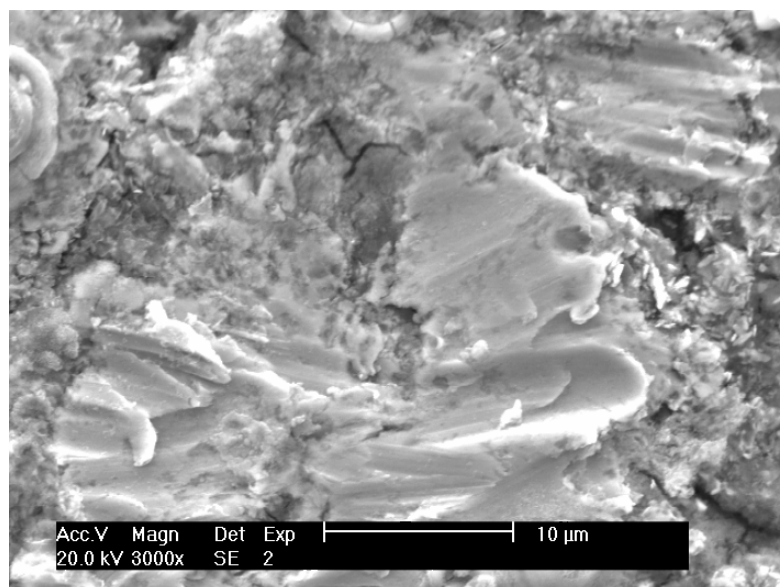


Figure 50. Specimen exposed to erosion-corrosion environment (3000X)

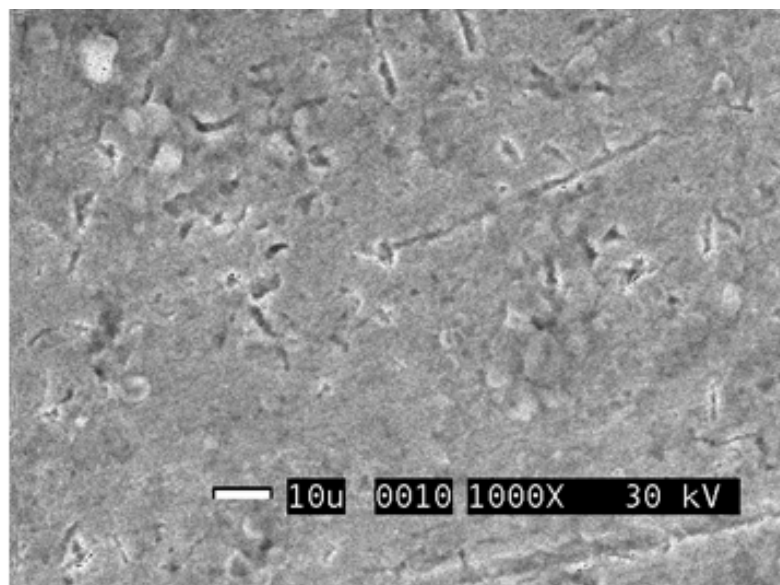


Figure 51. Specimen after pure corrosion²⁹ (1000 X)

Future work

The following are suggestions for future work:

1. Since the design of the test section is generic, it can be used to test different materials (for example 13% Cr steel) in either erosion, corrosion, or erosion-corrosion conditions.
2. Studies can be done by varying parameters like velocity, temperature, pH, and sand properties.
3. Increasing the length of the experiments may be helpful in understanding the processes and their interactions more clearly. However, it should be noted that care should be taken to avoid the effect of sand degradation. Use of sand separators is a possible solution for this.
4. Minimizing the range of the sand size distribution may be helpful in obtaining more accurate results.
5. Effect of inhibitors on erosion or erosion-corrosion in disturbed flow conditions can be studied.
6. The design of the test section can be improved, and the following are noteworthy points
 - The length of the test section after the flow disturbances should be increased so that complete flow redevelopment occurs. CFD simulations at the desired flow conditions may be very helpful to achieve this.

- O-rings can be replaced by washers with similar physical and chemical properties, so that the small flow disturbances occurring near the o-rings can be avoided.

CHAPTER 9 CONCLUSIONS

1. The unique, new design of the test section permits the erosion-corrosion study in realistic disturbed flow conditions.
2. A new approach was devised by which the contributions of both corrosion and erosion towards synergism were separated and quantified.
3. In a combined erosion-corrosion process, corrosion and erosion enhance one another resulting in significant synergism.
4. Enhancement of erosion by corrosion is the dominant mechanism for synergism.

REFERENCES

1. Neville A., and Hodgkiess T., "Study of effect of liquid corrosivity in liquid-solid impingement on cast iron and austenitic stainless steel," BRITISH CORROSION JOURNAL, 1997, vol. 32, n 3, page no. 197
2. Neville, A., Hodgkiess T., and Dallas J.T., "A study of the erosion-corrosion behavior of engineering steels for marine pumping applications," p 497, WEAR 186-187, 1995, page no. 497-507
3. Burstein G.T., Sasaki k., "Effect of impact angle on the erosion-corrosion of 304L stainless steel," WEAR 186-187, 1995, page no. 80-94
4. Zhou S., Stack M.M. and Newman R.C., "Characterization of synergistic effects between erosion and corrosion in an aqueous environment using electrochemical techniques," CORROSION SCIENCE 1996, vol. 52, n 12, page no. 934
5. Wang H.W., and Stack M.M., "The erosive wear of mild steel and stainless steels under controlled corrosion in alkaline slurries containing alumina particles," JOURNAL OF MATERIAL SCIENCE 2000, Vol. 35, page no. 5263-5273
6. Yugui Zheng, Zhiming Yao, Xiangyun Wei, Wei Ke, "The synergistic effect between erosion and corrosion in acidic slurry medium," WEAR 186-187, 1995, page no. 555-561
7. Madsen B.W., "Measurement of erosion-corrosion synergism with a slurry wear test apparatus," WEAR OF MATERIALS 1987, Vol. 2, page no. 777-786
8. Hubner W., and Leitel E., "Peculiarities of erosion-corrosion processes," TRIBOLOGY INTERNATIONAL 1996, Vol. 29, n 3, page no. 199
9. Wood R.J.K., and Hutton S.P., "The synergistic effect of erosion and corrosion: trends in published results," WEAR 140, 1990, page 387-394
10. Watson S.W., Friedersdorf F.J., Madsen B.W., and Cramer S.D., "Methods of measuring wear-corrosion synergism," WEAR 181-183, 1995, page no. 476-484
11. Lotz U., and Postlethwaite, J., "Erosion-corrosion in disturbed two phase liquid/particle Flow," CORROSION SCIENCE 1990, Vol. 30, n 1, page no. 95

12. Blatt, W., Kohley T., Lotz U. and Heitz E., "The influence of hydrodynamics on erosion-corrosion in two-phase liquid-particle flow," CORROSION SCIENCE 1989, Vol. 45, n 10, page no. 793
13. Nestic, S. and Postlethwaite, J., "Erosion in Disturbed Liquid/Particle Pipe Flow: Effects of Flow Geometry and Particle Surface Roughness," p 850, CORROSION ENGINEERING 1993, Vol 49, n 10, page no.850
14. Benedetto B., Marc, R.E., Marco B., and Claudio M., "Evaluation of erosion-corrosion in multiphase flow via CFD and experimental analysis," WEAR 225, 2003, page no. 237-245
15. Kermani M. B. and Morshed A., "Carbon dioxide corrosion in oil and gas production-a compendium," Corrosion 2003, Vol.59, No. 8, page no. 659
16. Nestic S., Postlethwaite J., and S. Olsen, "An electrochemical model for prediction of CO₂ corrosion," CORROSION 1995, paper no. 131
17. Salama M.M., "Influence of sand production on design and operations of piping systems," CORROSION 2000, paper no. 80
18. McLaury B.S., Shirazi S.A., Shadley J.R., and Rybicki E.F., "Parameters affecting flow accelerated erosion and erosion-corrosion," CORROSION 1999, paper no. 120
19. Finnie I., "Some reflections on the past and future of erosion," WEAR 186-187, 1995, page no. 1-10
20. Alan L.V., "Solid particle erosion and erosion-corrosion of materials," ASM INTERNATIONAL, c 1995
21. Meng, H.C., and Ludema, K.C., "Wear models and predictive equations: their form and content," WEAR 181-183, 1995, page no. 443-457
22. Nestic S., Nordsveen M., Nyborg R., and Stangeland A., "A mechanistic model for carbon dioxide of mild steel in the presence of protective iron carbonate films – part 1: theory and verification," Corrosion 2003, Vol. 59, n 5, page no. 443
23. Hamzah R., Stephenson D.J., and Strutt J.E., "Erosion of material used in petroleum production," WEAR 186-187, 1995, page no. 493-496

24. Postlethwaite J., "Effect of chromate inhibitor on the mechanical and electrochemical components of erosion-corrosion in aqueous slurries of sand," CORROSION 1981, Vol. 37, n 1, page no. 1
25. Matsumura M., oka Y., Hiura H., and Yano M., "The role of passivating film in preventing slurry erosion-corrosion of austenitic stainless steel," ISIJ Int. 1991, Vol. 31, n 2, page no. 168-176
26. Burstein G.T., Li Y., and Hutchings I.M., "The influence of corrosion on the erosion of aluminum by aqueous silica slurries," WEAR 186-187, 1995, page no. 515-522
27. Neville A., Reyes M. and Xu H., "Examining corrosion effects and corrosion/erosion interactions on metallic materials in aqueous slurries," TRIBOLOGY INTERNATIONAL 2002, vol. 35, page no. 643-650
28. Denny A. Jones, "Principles and prevention of corrosion," Chapter 5, second edition, Prentice Hall, c1996
29. Marc, S., et al., "Top of the line corrosion project report," Institute for Corrosion and Multiphase Technology, Ohio University, November 2004

APPENDIX A CALCULATIONS AND ANALYSIS OF LPR DATA

Analysis of LPR data

The anodic and cathodic tafel slopes β_a and β_c are functions of temperature. They can be expressed as:

$$\beta_a = \frac{2.303RT}{\alpha_a F} \quad (\text{A-1})$$

$$\beta_c = \frac{2.303RT}{\alpha_c F} \quad (\text{A-2})$$

where,

T is Absolute temperature in K, R is the universal gas constant (8.314 J/mol K), and α_a and α_c are the symmetry factors for anodic and cathodic reaction. The values of α_a and α_c are typically 1.5 and 0.5, respectively. F is Faraday's constant (96,500 coulombs/equivalent).

From the above equations the 'B' value can be calculated using the following expression:

$$B = \frac{\beta_a \beta_c}{2.303(\beta_a + \beta_c)} \quad (\text{A-3})$$

From the above equations (A-1, A-2, A-3), the average value of the 'B' value (B) in the temperature range of 20 °C - 100 °C was calculated to be 17.3 mV.

The corrosion rate was monitored using the linear polarization resistance (LPR) techniques. From basic electrochemical theory, the corrosion current density i_{corr} (A/m²) can be described as:

$$i_{corr} = B \times \frac{1}{R_p} \times \frac{1}{A} \quad (\text{A-4})$$

where,

B is the 'B' value explained above, R_p is the corrosion resistance in Ohms, and A is the working electrode surface area in m^2 .

The corrosion rate (CR) in mm/yr can then be calculated according to the following equation:

$$CR = \frac{m}{At\rho} = \frac{i_{corr}M_w}{\rho nF} = 1.16i_{corr} \quad (\text{A-5})$$

where,

m is the metal loss in kg, t is the time in seconds, ρ is the density of the material in kg/m^3 ,

M_w is the molecular weight of iron, F is the Faraday constant, n is the number of electrons exchanged in the electrochemical reaction.

APPENDIX B WEIGHT LOSS CALCULATIONS

The weight loss for each specimen is determined and the corrosion rate is obtained using the following equation,

$$CR = \frac{M \times 24 \times 365 \times 10}{\rho \times A} \quad (\text{B-1})$$

where,

CR = Corrosion rate in mm/yr

M = Mass loss in g/hr

ρ = Density in g/cm³

A = Area in cm²

APPENDIX C EXPERIMENTAL UNCERTAINTY ANALYSIS

The factors that affect the accuracy of the corrosion rate measurements and calculations include temperature, applied current, applied potential and the working electrode area.

According to the treatment shown in Appendix A, corrosion rate can be written as,

$$CR = 1.16i_{corr} \quad (C-1)$$

where corrosion rate (CR) is expressed in mm/yr, and i_{corr} is in A/m^2

Substituting (A-3) and (A-4) into (C-1) we get,

$$CR = 0.505 \frac{\beta_a \beta_c}{(\beta_a + \beta_c)} \times \frac{1}{R_p} \quad (C-2)$$

Since, β_a and β_c are dependent only on and vary linearly with temperature (Equation A-1, A-2), they can be rewritten as follows:

$$\beta_a = \beta_{a0} + m_1 T \quad (C-3)$$

$$\beta_c = \beta_{c0} + m_2 T \quad (C-4)$$

where, β_{a0} and β_{c0} are the base anodic and cathodic tafel constants at a suitable reference temperature. The slopes m_1 and m_2 can be easily obtained by plotting equations (A-1) and (A-2). The values obtained are $m_1 = 0.14$ mV/K and $m_2 = -0.4$ mV/K.

In equation (C-2), R_p can be expressed as follows:

$$R_p = \frac{dE}{di_{app}} \quad (C-5)$$

where, i_{app} is the applied current density in A/m^2

$$i_{app} = \frac{I_{app}}{a} \quad (C-6)$$

where, I_{app} is the applied current in A and a is the working area in cm^2

Substituting equation (C-3) to (C-6) in equation (C-2), we get

$$CR = 0.505 \frac{(\beta_{a0} + m_1 T)(\beta_{c0} + m_2 T)}{\beta_{a0} + \beta_{c0} + (m_1 + m_2)T} \times \frac{\Delta I_{app}}{\Delta E \Delta a} \quad (C-7)$$

Equation (C-7) can then be written in the following form:

$$CR = 0.505(\beta_{a0} + m_1 T)(\beta_{c0} + m_2 T)[\beta_{a0} + \beta_{c0} + (m_1 + m_2)T](\Delta I_{app})(\Delta E)^{-1}(\Delta a)^{-1} \quad (C-8)$$

The sensitivity of small changes in the corrosion rate to small changes in each variable is expressed by taking partial derivatives of the corrosion rate with respect to each variable. The errors in β_{a0} , β_{c0} , m_1 and m_2 are assumed to be negligible. Thus, the absolute uncertainty in the measurement of corrosion rate because of uncertainties in the system variables can be expressed as follows:

$$\frac{\delta(CR)}{CR} = \left[\frac{\partial(CR)}{\partial T} \right] \frac{\delta T}{CR} + 2 \left[\frac{\partial(CR)}{\partial E} \right] \frac{\delta E}{CR} + 2 \left[\frac{\partial(CR)}{\partial I_{app}} \right] \frac{\delta I_{app}}{CR} + 2 \left[\frac{\partial(CR)}{\partial a} \right] \frac{\delta a}{CR} \quad (C-9)$$

Deriving the partial derivatives of each item above according to equation (C-8) and then substituting into (C-9), the following equation is obtained:

$$\frac{\delta(CR)}{CR} = \left(\frac{m_1}{\beta_a} + \frac{m_2}{\beta_c} \right) \delta T - \frac{2}{E} \delta E + \frac{2}{I_{app}} \delta I_{app} - \frac{2}{a} \delta a \quad (C-10)$$

Therefore, the corrosion rate uncertainty above can be considered an overall uncertainty through the experiment for LPR techniques. It considers the uncertainties due to the temperature, instrumentation (potential and applied current), and the working

electrode surface area. The contribution of each item in (C-10) to the corrosion rate uncertainty measurements is calculated as follows:

Temperature

The temperature during the experiment was maintained at $34\text{ }^{\circ}\text{C} \pm 1\text{ }^{\circ}\text{C}$, thus $\delta T=1$. Tafel slopes calculated at $34\text{ }^{\circ}\text{C}$ are, $\beta_a = 60\text{ mV}$ and $\beta_c = 120\text{ mV}$. Hence the first part on the right hand side of the equation (C-10) is:

$$\left(\frac{m_1}{\beta_a} + \frac{m_2}{\beta_c}\right)\delta T = \left(\frac{0.14}{60} + \frac{-0.4}{120}\right) \times 1 = -1 \times 10^{-3} \quad (\text{C-11})$$

Potential

According to Gamry, the DC accuracy in voltage measurement is $\pm 0.3\%$ in $\pm 1\text{ mV}$ range. During the experiment, the applied potential was $\pm 5\text{ mV}$ over the open circuit potential. Thus the uncertainty in the potential would be $\delta E = 0.15\text{ mV}$.

Current

According to Gamry, the DC accuracy in current measurement is $\pm 0.3\%$ range $\pm 50\text{ pA}$. The current range was different for different experiments, and it varied with time because of the change in the corrosion rate. At the start of the experiment, the applied current range is usually around $400\text{ }\mu\text{A}$. Thus uncertainty in the current would be:

$$\delta I_{app} = 4 \times 10^{-4} \times 0.003 = 1.2 \times 10^{-6}\text{ A} \quad (\text{C-14})$$

Hence, the absolute uncertainty in equation (C-10), due to the current would be:

$$\frac{2}{I_{app}} \delta I_{app} = \frac{2}{4 \times 10^{-4}} \times 1.2 \times 10^{-6} = 6.0 \times 10^{-3} \quad (\text{C-15})$$

Hence, the error in corrosion rate due to the current is found from the above equation.

Electrode Area

The uncertainty in the area was due to the accuracy of the measuring instrument, the loss of area due to the polishing of the sample, and corrosion loss of the reused sample. It was estimated to be 0.1 cm^2 . Therefore, the absolute uncertainty due to the surface area in equation (C-10) for smaller a specimen is:

$$\frac{2}{a} \delta a = \frac{2}{38.38} \times 0.1 = 5.2 \times 10^{-3} \quad (\text{C-16})$$

For a larger specimen it is, $\frac{2}{61.2} \times 0.1 = 3.2 \times 10^{-3}$

The average uncertainty can be taken as the average value, 4.2×10^{-3}

Thus the uncertainties in the corrosion rate measurement from the LPR techniques for the specified experiment are expressed as:

$$\frac{\delta(CR)}{CR} = \pm \left(-1 \times 10^{-3} - \frac{2 \times 0.15}{5} + 6.0 \times 10^{-3} - 4.2 \times 10^{-3} \right) = \pm 6.8\% \quad (\text{C-17})$$

From the above equations, it can be concluded that in the LPR measurement techniques, the uncertainty in the potential is a major source of error in corrosion rate.

The error calculated in equation (C-17) would be the average error over the entire length of the experiment.

APPENDIX D CFD SETUP

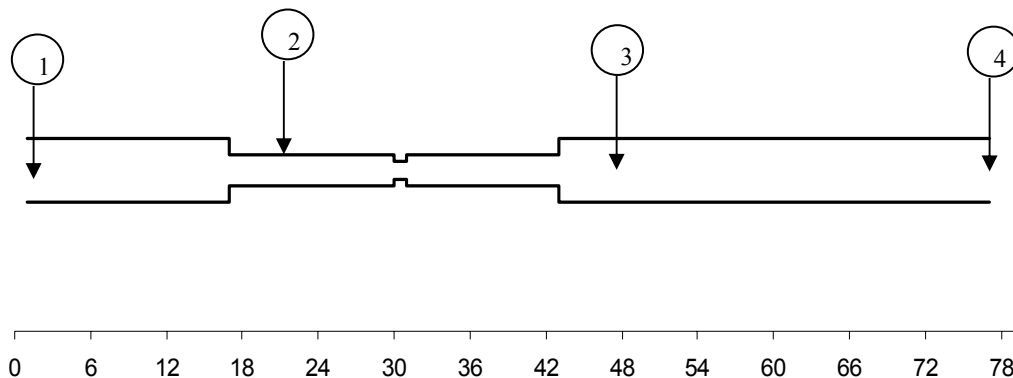
FLUENT

Version: 2d/3d, segregated.

Model	Settings
Time	Steady
Viscous	Standard k-epsilon turbulence model
Wall Treatment	Standard Wall Functions
Heat Transfer	Disabled
Solidification and Melting	Disabled
Species Transport	Disabled
Coupled Dispersed Phase	Enabled
Pollutants	Disabled
Soot	Disabled

BOUNDARY CONDITIONS

Zone	Type
1	velocity-inlet
2	wall
3	fluid (water)
4	outflow (Flow rate weighting = 1)



For better simulation, the boundary condition, velocity-inlet is positioned approximately one foot before the actual inlet of the test section.

SOLVER CONTROLS

Equations solved

Equation	Solved
Flow	yes
Turbulence	yes

Numerics

Numeric	Enabled
Absolute Velocity Formulation	yes

Relaxation

Variable	Relaxation Factor
Pressure	0.30000001
Density	1
Body Forces	1
Momentum	0.69999999
Turbulence Kinetic Energy	0.80000001
Turbulence Dissipation Rate	0.80000001
Turbulent Viscosity	1
Discrete Phase Sources	0.5

Discretization Scheme

Variable	Scheme
Pressure	Standard
Pressure-Velocity Coupling	SIMPLE
Momentum	Second Order Upwind
Turbulence Kinetic Energy	Second Order Upwind
Turbulence Dissipation Rate	First Order Upwind

MATERIAL PROPERTIES

Material: water-liquid (fluid)

Property	Units	Method	Value(s)
Density	kg/m ³	constant	998.2
Cp (Specific Heat)	J/kg-K	constant	4182
Thermal Conductivity	W/m-K	constant	0.6
Viscosity	kg/m-s	constant	0.001003
Molecular Weight	kg/kg-mol	constant	18.0152
L-J Characteristic Length	angstrom	constant	0
L-J Energy Parameter	k	constant	0
Thermal Expansion Coefficient	1/k	constant	0
Degrees of Freedom		constant	0

Material: silicon (inert-particle)

Property	Units	Method	Value(s)
Density	kg/m ³	constant	2000
Cp (Specific Heat)	J/kg-K	polynomial	(300-1000: 170.11206 3.0387201 -0.0052555797 4.3146586e-06 -1.3295637e-09) (1000-2500: 749.04106 0.25229083 -9.5424799e-05 3.7916328e-08 -5.4790954e-12)
Thermal Conductivity	W/m-K	constant	0.0454
Viscosity	kg/m-s	constant	1.72e-05
Molecular Weight	kg/kg-mol	constant	28.086
Thermal Expansion Coefficient	1/k	constant	0